MAPPING OF PASSIVE TURBULENCE CONTROL TO FLOW INDUCED MOTIONS OF CIRCULAR CYLINDERS

by

Hongrae Park

A dissertation submitted in partial fulfillment
of the requirements of the degree of
Doctor of Philosophy
(Mechanical Engineering)
in The University of Michigan
2012

Doctoral Committee:

Professor Michael M. Bernitsas, Chair
Professor Steven L. Ceccio
Professor Noel C. Perkins
Professor Armin W. Troesch

2012

DEDICATION

To my parent,

Yun Hwang Park, and Im Joo Lee

ACKNOWLEDGEMENTS

This dissertation would not have been possible without the guidance and assistance of several individuals who advised me and provided their valuable experience and contributed their time and effort in the preparation and completion of this study.

First and foremost I offer my sincerest gratitude to my supervisor, Professor Michael M. Bernitsas, for his excellent guidance, caring, diligence and support throughout my research. He tried to give every answer as I hurdle all the obstacles in the completion this research work. His support and guidance made me develop personally and academically.

I am grateful to my committee members, Professor Steven L. Ceccio, Professor Noel C. Perkins, and Professor Armin W. Troesch. Their advice was crucial toward completing my work, and made me notice weaknesses in my research.

This thesis would not have been possible without my family's support. I owe my deepest gratitude to my parents, Yun Hwang Park and Im Joo Lee. I am really lucky to have great parents. Their encouragement and unconditional love are the reason I managed to overcome many challenges in my life. I always appreciate and never forget their support and love. I also would like to thank my brother Sang Rae Park, my sister-in-law So Hyun Park, nephews Chae Yeon (Estelle) Park, and Ji Ho (Brandon) Park. They help me appreciate how precious family values are. I would not be where I am today without my family.

It is a pleasure to thank our VIV group who made this study possible. I would like to thank our team members, Che-Chen (Jim) Chang and his wife Tina Chen, Eun Soo Kim, Jonghun Lee, Ajith Kumar Raghavan, and Wei Wu. It has been my pleasure working with them in the past four years. They are not only good lab-mates but also good friends for life.

I am grateful to NA&ME students, Eun Jung Chae, Ayoung Kim, Dae-Hyun Kim, Hong Yoon Kim, and In-ho Lee. I share good memories with them that made me happy through my graduate studies.

I would like to express my gratitude to my friends outside of University of Michigan: Hyeon-Ju Cho, Youseok Go, Dongyun Han, Neil Hodges, his wife Mary Hodges, Dongjin Hyun, Minsung Jo, Hyunkoo Kang, Se Kyoung Kim, Hyun Sik Kwon, Dongkyung Lee, Jae Hong Lee, Seung-Hwan Lee, Wang Ho Lee, Joo Yeob Nam, Meong Cheol Shin, Kyungjun Song, Judith Yi, and Jaewon Yoon. I gained valuable memories by sharing my life with them. I appreciate their willingness to help me when I was in need.

I would like to thank College of Engineering, and the department of Naval Architecture and Marine Engineering, University of Michigan, for their fellowships during my graduate studies.

The following support is gratefully acknowledged: (1) ONR grant N00014-03-1-0983 to the University of Michigan, Program Manager Kelly Copper. (2) ONR grant N00014-08-1-0601 to the University of Michigan, Program Manager Kelly Copper. (3) NSF-SBIR grant to Vortex Hydro Energy and the University of Michigan award # IIP-0810426, Program Manager William Haynes.

Finally, I would like to thank everyone who made contribution directly and indirectly

to my studies and life. Also, I would like to convey my apology to all the important people that I failed to acknowledge by name in this relatively short statement.

TABLE OF CONTENTS

LIST OF FIGURES

LIST OF TABLES

GLOSSARY

Roman symbols

A	maximum value of the transverse displacement
A^*	amplitude ratio A/D, average of the 60 highest peaks; 10-20 peaks are averaged in suppression since more may not be available.
c	structural damping
C_A	potential flow added-mass coefficient of a circular cylinder (C_A=1.0)
C_D	drag coefficient
C_L	lift force coefficient
$C_{potential}$	potential force coefficient
C_{total}	instantaneous transverse force coefficient = $\frac{F_{total}}{\frac{1}{2}\rho U^2 DL}$
C_{vortex}	vortex force coefficient
$\overline{C_{total}}$	maximum transvers force coefficient
D	diameter of cylinder
f_N	natural frequency = $\frac{1}{2\pi}\sqrt{\frac{K}{m}}$
$f_{N,w}$	natural frequency in water = $\frac{1}{2\pi}\sqrt{\frac{K}{m+m_a}}$
f_{osc}	body oscillation frequency
f_v	vortex-shedding frequency for stationary cylinder
f_w	wake vortex mode
f^*	oscillation frequency ratio = $\frac{f_{osc}}{f_{n,w}}$
F	instantaneous Fluid force
F_D	drag force
F_L	lift force
F_{max}	maximum fluid force
$F_{potential}$	instantaneous potential force in transverse direction
F_{total}	instantaneous total force in transverse direction
F_{vortex}	instantaneous vortex force in transverse direction
k	roughness grit size
K	spring constant

l_f	vortex formation length
L	cylinder length
L'	center to center distance between cylinders
m	oscillating mass
m_a	added mass
$m_{cylinder}$	mass of cylinder
m_d	displaced fluid mass
m^*	mass ratio
H	sieve thickness of PTC in mm,
HG1, HG2	hard galloping zones; galloping initiated by initial threshold displacement of one diameter ($1 \bullet D$)
PTC	Passive Turbulence Control
P60:20°-36°	two symmetric strips P60 with leading edge at ±20° and 16° width
Re	$= UD/v$ Reynolds number
SG	soft galloping zone; self-initiated galloping
SS	strong suppression zone; suppression of response amplitude is between 0% and75% of the corresponding smooth cylinder amplitude
St	Strouhal number $= f_v^* D/U$
t	time
T	a period of cylinder oscillation
U	flow velocity
U_{rel}	relative velocity between cylinder motion and free stream velocity
U^*	reduced velocity $= \dfrac{U}{f_{N,w} D}$
Vn	n^{th} generated vortex
WS1, WS2	weak suppression zones; maximum amplitude of response is no less that 75% of the corresponding smooth cylinder amplitude
y	instantaneous cylinder motion in transvers direction

Greek symbols

α	angle of attack
α'	cylinder orientation angle in x-y coordinate
α_{PTC}	PTC placement angle measured from front
δ	boundary layer thickness

ζ	structural damping ratio
θ_c	critical angular position where Strouhal number drops steeply
θ_p	perturbation angular position
θ_r	angular position where Strouhal number recovers
μ	fluid dynamic viscosity
ν	fluid kinematic viscosity
ρ	water density at 15°C
ϕ	phase angle between two cylinder motions
ϕ_{total}	phase angle between total lift force and cylinder motion
ϕ_{vortex}	phase angle between vortex lift force and cylinder motion
ω_n	undamped natural frequency of the system in vacuum

ABSTRACT

Passive turbulence control (PTC) in the form of selectively distributed surface roughness is applied on a rigid circular cylinder on two end-springs. The cylinder is placed horizontally with its axis perpendicular to a uniform steady flow and is allowed one degree of freedom in the vertical direction. PTC consists of two roughness strips placed parallel to the cylinder axis and symmetrically to the flow with thickness on the order of the boundary layer thickness. Broad field-of-view flow visualization is used to study the wake vortex patterns.

Amplitude and frequency response are measured experimentally in the range of $3\times10^4 \leq Re \leq 1.2\times10^5$ for broad ranges of the main PTC parameters. Lift force and force-displacement lag are calculated from the time history of the displacement. Different flow induced motion (FIM) is observed depending primarily on the circumferential location of the two strips. A ***PTC-to-FIM Map*** is developed showing six distinct FIM zones: two weak-suppression and one strong-suppression zones in vortex induced vibration, a soft galloping zone and two hard galloping zones in galloping. All zones exhibit robustness with respect to roughness strip width and thickness, and even change in strip configuration. In galloping, amplitudes of oscillation reach 2.9 times the cylinder diameter limited only by the free-surface and bottom-boundary of the experimental flow channel. Visualization shows some of the conventional, low Reynolds number patterns like 2S and 2P, as well as more complex patterns with up to ten vortices per cycle.

The developed ***PTC-to-FIM Map*** is useful in suppressing FIM to prevent structural damage as well as enhancing FIM to convert more hydrokinetic energy to mechanical and subsequently to electrical energy. Based on the ***PTC-to-FIM Map***, suppression models using PTC are designed for flow-direction dependence and independence for a single cylinder. Both the amplitude and synchronization range were reduced. Two cylinder systems were also tested for FIM interference.

CHAPTER 1

INTRODUCTION

1.1. MOTIVATION

Fluid-Structure Interaction (FSI) of a flexible cylinder or a rigid cylinder on end-springs in a steady transverse flow is a phenomenon occurring frequently in a multitude of engineering applications such as heat exchangers, cooling towers, bridges, buildings, and offshore structures. Among flow-induced motions, the most commonly occurring phenomenon is Vortex Induced Vibrations (VIV). Nevertheless, other phenomena such as galloping, flutter, and buffeting are also encountered in practice.

As a direct consequence of FSI, oscillatory motions may be induced in structures if they are flexible or flexibly supported. These Flow Induced Motions (FIM) could adversely affect the safety of structures by shortening their service life (Paidoussiss 2006). Efforts to suppress FIM have been expended in the past and still continue (Kumar et al. 2008). Research on developing both passive and active control to attenuate FIM is ongoing (Muddada & Patnaik 2010; Zdravkovich 1981).

On the other hand, power of FIM has drawn attention as a means to harness renewable energy. From a recent study by the MRE (Marine Renewable Energy) lab at the University of Michigan, FIM can be used to convert marine hydrokinetic energy to

mechanical and subsequently renewable electrical energy. The VIVACE (Vortex Induced Vibrations for Aquatic Clean Energy) converter invented by Bernitsas & Raghavan (2007) extracts hydrokinetic energy from a flow current using VIV. From a study by Chang (2011), galloping enhances the cylinder motion at high reduced velocity where a smooth cylinder would be in the VIV desynchronization region. The efforts by Bernitsas and his team at the University of Michigan to harness marine hydrokinetic energy using FIM still continues (Bernitsas et al. 2006a,b; Bernitsas & Rakhavan 2007, 2008, 2009, 2011; Chang & Bernitsas 2011; Chang et al. 2011; Kim et al. 2011; Lee & Bernitsas 2011; Lee et al. 2011; Raghavan & Bernitsas 2007a,b, 2011).

Presently, two different and contrasting interests in FIM are important for engineering applications. The goal in this dissertation is to study experimentally, for a broad range of parameters, an effective yet simple device, which can act as a FIM suppressor as well as an amplifier depending on the application at hand. That is, (a) to devise a passive means to suppress the flow induced motions in line with conventional practice on structural safety (Kumar et al. 2008) and (b) to devise a means to augment cylinder oscillations to convert more hydrokinetic energy to mechanical and subsequently electrical energy.

Studies by Bernitsas et al. (2006, 2007, 2009) on the effect of Passive Turbulence Control (PTC) on flow induced motions of a circular cylinder indicate that selectively applied roughness could cause substantial changes in the boundary layer characteristics and thereby on the cylinder response. In their quest to harness more and more energy from the fluid flow, they have observed that application of roughness resulted in significant amplification of the cylinder response, compared to a single smooth cylinder. In the light of their studies, it is thought that if roughness could amplify the oscillations, it

could bring amplitude reduction if applied differently and act as a suppression device. One of the aims of the present study is to address this issue of FIM suppression.

Furthermore in previous studies, Bernitsas et al. (2007, 2008, 2009) and Chang et al. (2011) introduced motion enhancements and studied the cylinder FIM only for some selected circumferential locations of roughness. One of the goals of the present study is the extension of the roughness application over a broader range of circumferential locations. Hence, the cylinder response based on the roughness location and height will be classified. As aforementioned, the present study aims at suppression and enhancement of FIM. It is worthy to note that even though there are many studies revealing the effect of surface roughness on flow around a circular cylinder (Achenbach 1971; Achenbach & Heinecke 1981; Güven et al. 1980; Nakamura & Tomonari 1982), roughness is not perceived as a possible means of suppression.

In this research, Passive Turbulent Control (PTC) is studied experimentally. PTC consists of roughness applied in the form of two straight sandpaper strips, located symmetrically on its surface with respect to the flow, running along the entire cylinder span. Therefore, the major objective of this dissertation is the response classification and mapping based on the application of PTC.

The following questions are addressed as part of the basic problem formulation: (i) What is the effect of selectively distributed roughness on the FIM response of the cylinder, when compared with the FIM of a smooth cylinder? (ii) Is there any relationship between the cylinder response and the circumferential location of the roughness strip? (iii) Can the circumferential strip locations be classified into different zones based on the cylinder oscillatory response? (iv) What is the role of roughness height in case (iii) is

realized? (v) What are the possible flow structures responsible for the observed FIM and how are they related to each other?

Investigation on smooth and rough circular cylinders is carried out to answer the aforementioned questions.

1.2. LITERATURE REVIEW

1.2.1. Flow regime

Flow characteristics around a circular cylinder are highly dependent on Reynolds number. Roshko (1961) paid attention to flow separation and divided the flow regime into the subcritical range (laminar boundary layer separation), the supercritical range (laminar separation followed by turbulent reattachment and turbulent separation), and the transcritical range (transition to turbulence in the boundary layer occurring ahead of separation). Achenbach (1977) and Farell (1981) used boundary characteristics to sort the flow regimes, and supplemented the flow regime by adding the critical range as shown in Fig. 1.1. In Fig. 1.1, the total drag coefficient is associated with boundary layer separation and flow transition from laminar to turbulent since the total drag coefficient C_D can be calculated by the integration of the local values of static pressure and skin friction. For the turbulent boundary layer, turbulent momentum exchange give additional energy to the boundary layer and it overcomes the adverse pressure gradient. Thus, the separation point is delayed resulting in smaller drag coefficient, smaller width of the wake, and higher vortex shedding frequency than those of the laminar flow. The exact Reynolds number

region of laminar to turbulent boundary transition has not been defined precisely due to experimental uncertainties (Niemann & Hölscher 1990).

From Achenbach (1977) and Farell (1981), following overall observations are made for the flow past a smooth circular cylinder:

(i) In the subcritical flow region, the boundary layer is laminarly separated at around 70°-80° from the front stagnation point and the drag coefficient is independent of Reynolds number.

(ii) In the critical range, transition from laminar to turbulent separation is observed. At first, the boundary layer is in laminar separation and after the transition, turbulent reattachment occurs with "separation bubble". Finally turbulent separation occurs. Sudden drop of the drag coefficient and the critical Reynolds number where the drag coefficient is minimum are found. According to Schewe (1983), boundary layer transition may be more complicated as shown in Fig. 1.2.

(iii) In the supercritical flow region, a separation bubble exists and the separation point is delayed until around 140° from the front stagnation point. The drag coefficient is almost constant.

(iv) In the transcritical flow region, the separation bubble disappears and turbulent separation occurs at around 110° from the front stagnation point.

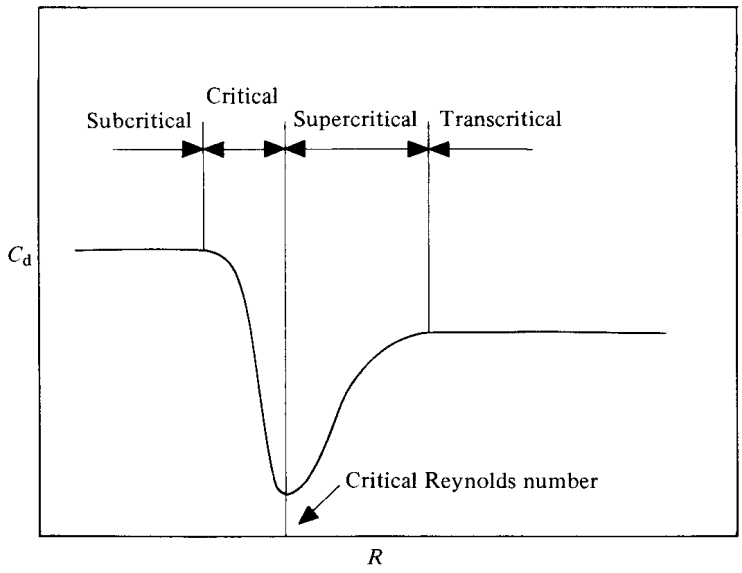

Fig. 1.1. Four Reynolds number ranges relevant to the flow past circular cylinders (Nakamura & Tomonari 1982)

	subcritical	critical					super-critical	trans-critical
			discontinuity A, hysteretic		discontinuity B, hysteretic		upper transition	
	(1)	(2)	(3)	(4)	(5)	(6)	(7)	(8)
state of boundary layer	stable		unstable	bistable	unstable	stable	unstable	stable
10^5 Re	1,4	2,8	3,0	3,3	3,5	10	50	
mean drag c_D	1,2	1,2 - 1,0	1,0 - 0,7	0,5	0,5 - 0,4	0,22	0,22 - 0,52	0,52
mean lift c_L	0			± 1,3	1,3 - 0,9	0	0,1 ... 0,2	0
fluctuating lift: SDF	single narrow peak		random with two peaks	narrow peak	random + peak	narrow peak	random, two broad peaks	rather narrow peak
Sr	0,2		0,2	0,33	0,31	0,48	(0,1/0,45)	0,28
$c_{L,rms}$	0,4 - 0,25	0,25 - 0,09	0,09 - 0,06	0,04	0,04 - 0,07	0,02	0,04	0,05
boundary layer and separation	laminar separation S_l	laminar separation	random changes	one-sided separation bubble	random changes	two-sided separation bubble	random changes	turbulent separation S_t

Fig. 1.2. Flow range classification by Schewa (1983)

As shown in Fig. 1.3, more detailed flow regimes around a circular cylinder are identifying based on transition in the wake, free shear layers, separation points, and boundary layers (Zdravkovich 1990). According to Zdravkovich, the flow regimes are subdivided as follow:

L1 - 'creeping' flow (no-separation) $0 < Re < 4$ to 5

L2 - steady separated region (closed near-wake) 4 to $5 < Re < 30$ to 48

L3 - periodic laminar wake 30 to $40 < Re < 150$ to 200

TrW1 - transition of laminar vortices in wake 150 to $200 < Re < 350$ to 500

TrW2 - transition of vortices during formation 200 to $250 < Re < 350$ to 500

TrSL1 - transition waves in free shear layers 350 to $500 < Re < 1k$ to 2k

TrSL2 - transition vortices in free shear layers 1k to $2k < Re < 20k$ to 40k

TrSL3 - fully turbulent shear layers 20k to $40k < Re < 100k$ to 200k

TrS0 - onset of transition on separation 100k to $200k < Re < 320k$ to 340k

TrS1 - single separation bubble regime 320k to $340k < Re < 380k$ to 400k

TrS2 - two-bubble regime 380k to $400k < Re < 500k$ to 1M

TrS3 - supercritical regime 500k to $1M < Re < 3.5M$ to 6M

TrBL4 - transcritical regime, 3.5M to $6M < Re < 6M$ to 8M

T1 - postcritical regime $Re > 8M$

T2 - ultimate regime Re close to infinity

with the notation L: Laminar in all regions of flow; TrW: Transition in wake, laminar elsewhere; TrSL: Transition in free shear layers, wake turbulent; TrS: Transition around separation, boundary layer laminar; TrBL: Transition in boundary layers; T: Turbulent in all regions of flow.

The flow regime in the present study is in TrSL3 for a smooth cylinder. Since surface roughness can produce local turbulence, the roughness has direct impact on the transition of the boundary layer state (Zdravkovich 1990). For a cylinder with PTC, the flow regime depends on the PTC location and may move up to TrS or TrBL in the present study.

Flow regions discussed in this section are highly dependent on Reynolds number. However, these regions could be affected by cylinder aspect ratio, end plate, blockage effects, turbulent intensity, and surface conditions (Güven et al. 1980). To compare with the results from other investigators, compensation for some of these aspects - such as blockage effects - is necessary.

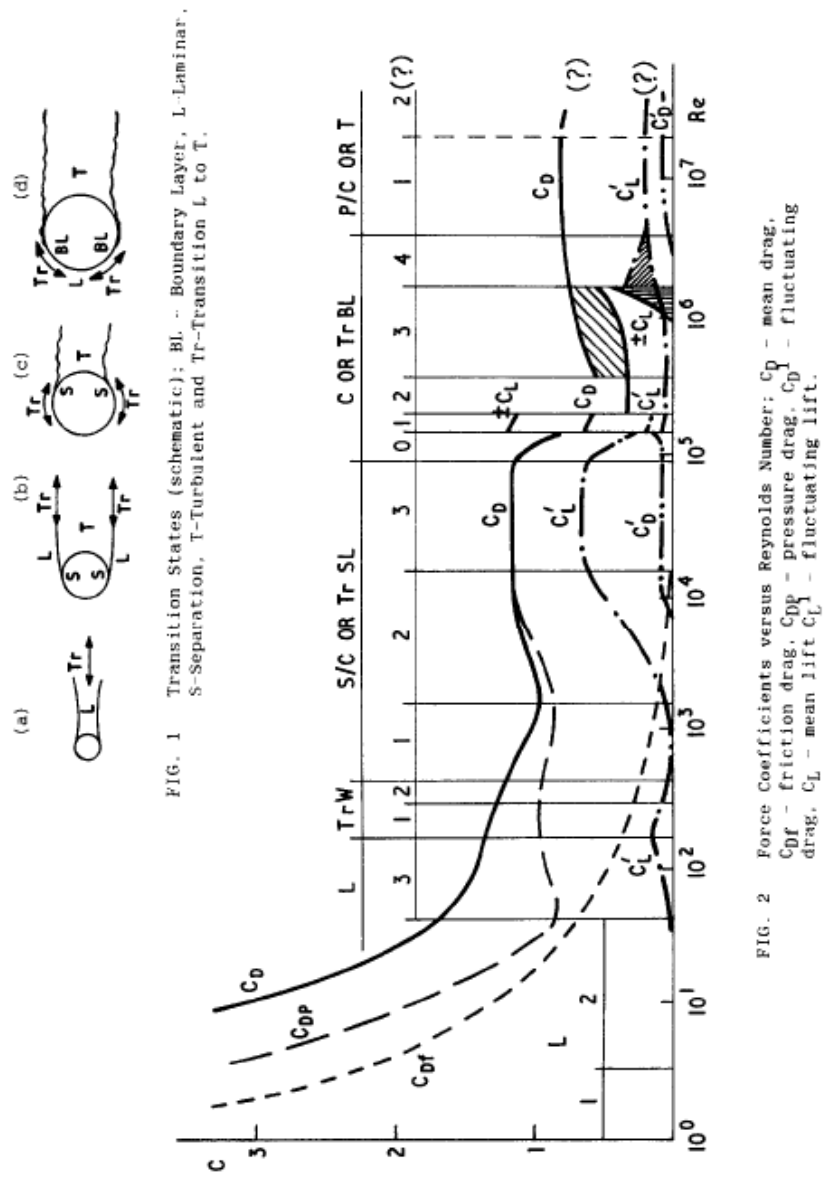

Fig. 1.3. Boundary layer transition state and force coefficients vs. Reynolds number (Zdravkovich 1990)

1.2.2. Surface roughness

Similarly to Reynolds number effect, surface roughness has a significant influence directly on the boundary layers and indirectly on the free shear layers. This influence eventually changes the mean pressure distribution and separation of the boundary layer (Achenbach 1977). Hence, roughness influences the vortex formation process.

Fage & Warsap (1930) demonstrated that the character of the boundary layer depends on Reynolds number and the surface condition of the cylinder. Achenbach (1971) used emery paper and 2.5mm sphere roughness on the surface of a circular cylinder to evaluate the total drag coefficient as function of Reynolds number and roughness parameter. Fage & Warsap (1930) and Achenbach (1971) showed that large roughness heights cause strong disturbances and therefore lead to premature transition decreasing the critical Reynolds number. Szechenyi (1975) used this fact to produce supercritical flows on cylinders using spherical roughness. Güven et al. (1980) studied the surface roughness effect on the drag coefficient, pressure distribution parameters, and boundary layer using commercial sandpaper, which has little larger grit size than the present study, and compared with literature results. The pressure rise at separation is closely related to the characteristics of a boundary layer. Larger roughness gives rise to a thicker and more retarded boundary layer causing earlier separation and a smaller pressure recovery. Achenbach & Heinecke (1981) studied the influence of surface roughness on the Strouhal number and boundary layer separation in critical, supercritical, and transcritical region. They found that as roughness increased in the critical region, (i) the minimum value of c_d at the critical Reynolds number increased and (ii) corresponding Strouhal number was smaller. The reason was that the boundary layer of the rough cylinder separated at earlier upstream position than that of the smooth cylinder.

For the uniformly distributed surface roughness the following conclusions have been published in the open literature as shown in Fig. 1.4:

(i) In the subcritical flow region, the boundary layer is laminar and the drag coefficient is almost constant regardless of surface roughness.

(ii) In the critical flow region, as the separation point of the laminar boundary layer moves downstream, a sudden drop in the drag coefficient is observed. As surface roughness is increased, the sudden drop in the drag coefficient becomes smaller, and the critical Reynolds number where the minimum drag coefficient is found is decreased. As higher roughness causes earlier separation, a higher drag coefficient is observed. A predominant vortex shedding frequency is not present in the critical regime.

(iii) In the supercritical flow region, turbulent separation occurs and the drag coefficient increases. This flow region is much reduced compared to the smooth cylinder and even not observed for the higher roughness values.

(iv) In the transcritical region, the boundary layer transits from laminar to turbulent near the front stagnation point and the drag coefficient is almost constant. If roughness is above a certain value, the drag coefficient is independent of the roughness.

A detailed review of the effect of uniformly distributed roughness and the flow regimes are provide by Farell & Arroyave (1990), Niemann & Hölscher (1990) and Zdravkovich (1990).

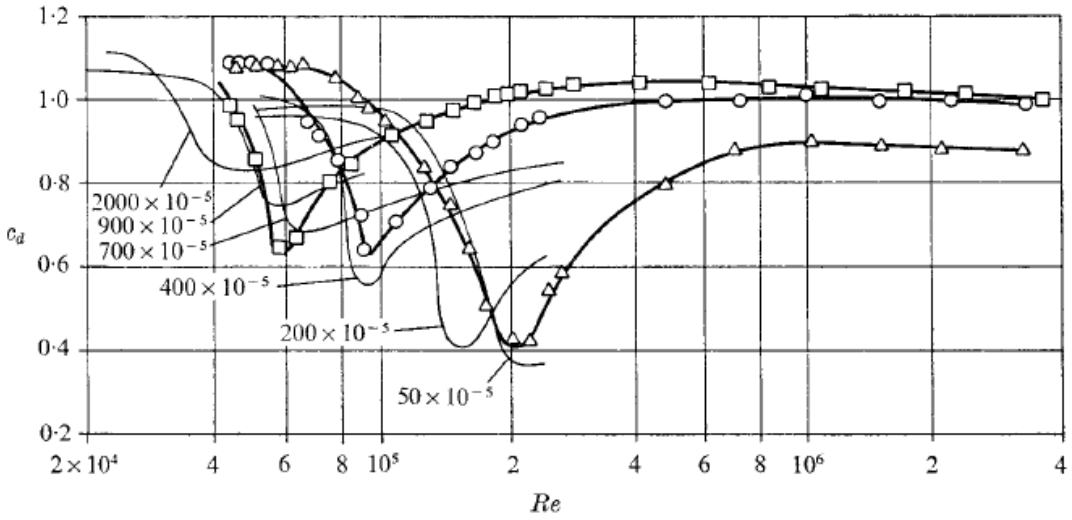

FIGURE 9. Corrected drag coefficient of rough circular cylinders in cross-flow. Comparison with results of Fage & Warsap (1930). △, $k_s/D = 110 \times 10^{-5}$; ○, $k_s/D = 450 \times 10^{-5}$; □, $k_s/D = 900 \times 10^{-5}$; ——, Fage & Warsap (1930).

Fig. 1.4. Drag coefficient of the roughness cylinder vs Reynolds numbers (Achenbach 1971)

Local roughness may have different effects than uniformly distributed roughness. Teverovskii (1968) investigated local roughness effect on Strouhal number. As seen in Fig. 1.5, he researched four roughness positions in symmetric pattern with different roughness sizes. For variant 1 (roughness at 66° from the front stagnation point), roughness about the thickness of the boundary layer was located in the area of the minimum pressure of the cylinder. Strouhal frequency was increased by the turbulence occurred in the boundary layer in the subcritical region. On the other hand, when the roughness height was greater than the boundary layer thickness, the boundary layer was separated from the cylinder, and the Strouhal number was decreased because of bigger volume of separated eddies than that of the smooth cylinder. For variant 2 (roughness at 114° from the front stagnation point), roughness was placed behind the separation point of the boundary layer and did not affect much the Strouhal frequency. For variant 3

(roughness at 26° from the front stagnation point), roughness was located in the area of the large negative pressure gradients, and Strouhal frequency was increased because of the earlier transition to turbulent and additional eddy caused by roughness. For variant 4 (one at 26° and the other at 66° from the front stagnation point), similar response to variant 1 was observed. When roughness height at 66° was higher than the boundary layer thickness, the amount of eddies was increased.

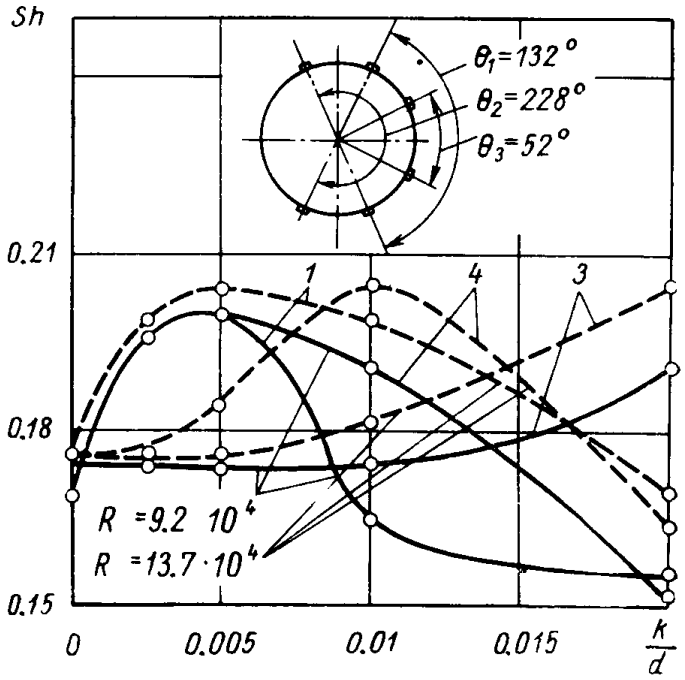

Fig. 1.5. Strouhal number as a function of the relative roughness k/d and the positions of the projections, which simulate the roughness: 1- variant 1(θ_1=132°); 3-variant 3(θ_3=52°); 4-variant 4(θ_1+ θ_3=184°)

For the systematic measure of the roughness effect and meaningful physical parameters, k/δ (ratio of roughness height to boundary layer thickness) should be used. However, the problem is that the boundary layer is a function of Reynolds number and the circumference location along the circular cylinder. Achenbach (1981) and Güven et al.

(1980) used effective roughness and Nakamura & Tomonari (1982) suggested similarity parameter in the form of $(r/D)^m R$ where r: roughness height, D: cylinder diameter, m: constant and R: Reynolds number. None of them were used widely. After all people used D (cylinder diameter) as auxiliary characteristic length for nondimensional variable. Thus, k/D is used as the only roughness variable in the present study.

1.2.3. Surface protrusions

Similarly to surface roughness, surface protrusions also have an effect on the flow around a circular cylinder. The effect of small protrusions such as tripping wires was first studied by Fage & Warsap (1930). They used thin wires smaller than the laminar boundary layer thickness and found that small thin wires could reduce the drag coefficient and change the pressure distribution around a stationary cylinder. Later, Igarashi (1986) researched the effect of tripping wire on boundary layer transition depending on different circumference locations on the circular cylinder. From his research, three distinct flow patterns – laminar boundary after reattachment (pattern A), turbulent boundary after reattachment (pattern C), and separation on wire without reattachment (pattern D)- are observed as seen in Fig. 1.6. In pattern C, the turbulence that occurred in the boundary layer has more momentum and reattaches with the final separation delayed. Thus the final separation point is delayed. The location of the tripping wire in pattern C which is similar to the critical flow is ±65° which is closely related to the laminar separation point.

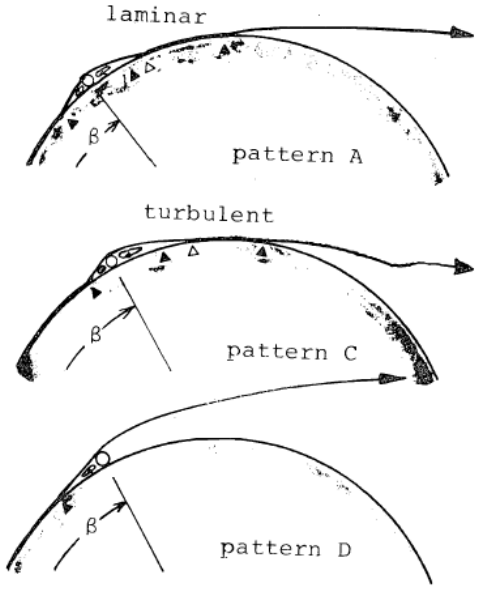

Fig. 9 Flow around roughness

Fig. 1.6. Different flow patterns around circular cylinder depending on wire location Igarashi (1986)

Nebres & Batill (1993) used several sizes of surface perturbation at various circumference locations on a stationary circular cylinder and also found similar flow patterns at similar location. As seen in Fig. 1.7, similar flow patterns to Fig. 1.6 were also observed at similar surface protrusion locations. Furthermore, they studied the effect of surface protrusion on Strouhal number, pressure distribution, lift and drag coefficients of the circular cylinder. Surface protrusion changes the separation point that is vortex formation process and consequently modifies the forces on the cylinder.

Hover et al. (2001) researched stationary and oscillating cylinders with tripping wires at ±70°. For the stationary cylinder, tripping wires decreased the drag and lift forces. For the oscillating cylinder, moderate amplitude with reduced lift force was observed compared to a smooth cylinder and even no excitation region was seen. The idea of tripping wire reducing the lift force gave some clue to VIV suppression. Alam et al.

(2003) and Kim et al. (2009) tried tripping rods, which had a considerably higher size than tripping wire, in VIV suppression for a single circular cylinder and two circular cylinders in tandem arrangements. They placed tripping rods at 20° to 60° from a stagnation point and found the optimum angle (30°) which caused the lowest lift force. They found three flow patterns depending on rods location. For pattern A (rods were placed between 20°-40°), boundary layer reattached with final laminar separation. For pattern B (rods were placed between 45°-60°), boundary layer separated at the rods and did not reattach to the cylinder surface. For pattern C (rods were placed between 41°-44°), a bistable flow state was observed. In other words, patterns A and B intermittently appeared.

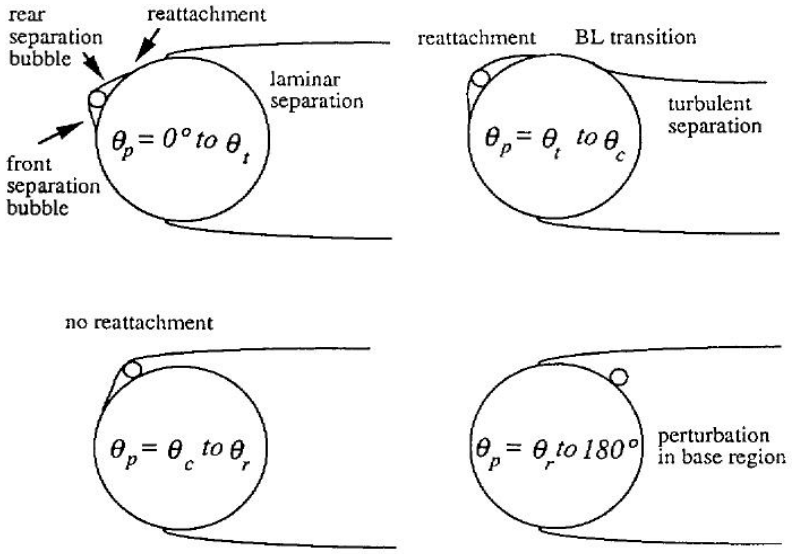

Fig. 1.7. Different flow regimes as function of the perturbation angular position (θ_p): Nebris & Batill (1993)

1.3. SOLUTION APPROACH: FIM PASSIVE TURBULENCE CONTROL

Solution to the problem defined in Section 1.1 is carried out by experimental means in this dissertation. A circular, hollow, aluminum cylinder with diameter D=3.5" (8.89cm) and length L=36" (91.4cm) is used in the experiments conducted to measure the oscillatory response features of the cylinder. Straight roughness strips with certain width are glued to the surface of the circular cylinder, which is otherwise smooth, at various circumferential locations starting from the front stagnation point. Two types of strips are used with significantly different roughness values. Roughness of the strip is indicated by the 'P' value of the sandpaper. The higher the P value, the lower is the roughness height (smoother). Accordingly, roughness strips P180 and P60 are applied in this study. Further details regarding roughness application and experimental set up are provided in Section 2.5. Broad field-of-view (FOV) visualization is used to explore the near-wake vortex structures of the cylinder and observe their relation to the cylinder FIM.

The approach method used in the present study is distinctive from previous studies of roughness or tripping wire in some points of view.

(i) Roughness is applied for only selective region of a cylinder surface. Achenbach (1971, 1977) Achenbach & Heinecke (1981), Güven et al. (1980) and Szechenyi (1975) studied roughness distributed around the whole cylinder and thus their experiments could not be used to find the effect of roughness position along the cylinder circumference.

(ii) A cylinder is mounted on linear springs. Previous studies involving surface roughness were mainly aimed at a stationary cylinder. Their core of studying was focused on only surface pressure distribution, a drag coefficient, flow separation and Strouhal number and their study was not concentrated on the hydrodynamic

excitation of the body. Nakamura & Tomonari (1982) investigated selective roughness covering only a narrow region and Nebres & Batill (1993) studied large perturbation at various locations and found that the perturbation position had a significant influence on pressure, Strouhal number, drag and lift forces. Their researches, however, focused only on a stationary cylinder.

(iii) Thickness of sandpaper is about the size of the boundary layer thickness. Suitable thickness of sandpaper is needed in tripping boundary layer and potentially changing a separation point at high Reynolds number.

(iv) In this study, the full range of PTC location on the cylinder surface and boundaries of zones are studied. Especially, boundaries between zones are very sensitive and can change the cylinder response dramatically. Hover et al. (2001), and Alam et al. (2003) also researched an oscillating cylinder with tripping wire only at a specific location. This tripping wire or single perturbation may have similar effect as roughness on a cylinder. Still their studies were confined on either a stationary cylinder or limited coverage range of tripping wire or large perturbation.

(v) From the results found in the present study, two variables are the most important factors affecting flow around a circular cylinder. One is height of PTC. Second is width of PTC. The advantage of PTC is that height and width of PTC are independent while a diameter change in tripping wires eventually alters a width together.

1.4. THESIS OUTLINE

The major objectives of the current study are as follows:

(a) To show PTC can be used in FIM enhancement/suppression

(b) To find zonal effect between PTC and FIM of circular cylinder

(c) To develop PTC suppression models that are flow direction dependent or independent

(d) To study the response of two smooth cylinders in tandem at high Reynolds numbers

(e) To create the suppression models of two tandem cylinders

The experimental set-up is described in Chapter 2 including the facility and the PTC, which is applied in the form of selectively distributed surface roughness. The smooth cylinder response in the range of Reynolds numbers considered in this work, $3\times10^4 \leq Re \leq 1.2\times10^5$, is established in Chapter 3. Each zone of mapping associated with a specific FIM response is established experimentally in Chapters 4-5. For each zone, (a) amplitude and frequency, (b) displacement time histories and power spectra, (c) near-wake vortex structures are presented and discussed. The *PTC-to-FIM Map* and the robustness of each zone with respect to parameter variation are presented in Chapter 6. In Chapter 7, design of PTC configuration in VIV suppression is studied and flow direction independent suppression device is also proposed. Covering multi-zone effect is presented in Chapter 8. In Chapter 9, a final suppression model designed from Chapter 7 and Chapter 8 is applied in two tandem cylinder experiments. The summary of conclusions is presented at the end.

CHAPTER 2

EXPERIMENTAL SETUP AND TEST MATRIX

In this chapter, the experimental apparatus and motion mechanism set-up are described first. Then, measurement details and flow visualization used to assess the FIM response are presented. Finally, the roughness configurations used to make up the Passive Turbulence Control in the tests are explained.

2.1. FACILITY – LOW TURBULENCE FREE SURFACE WATER CHANNEL

The experiments are conducted in the LTFSW (Low Turbulence Free Surface Water) Channel of the Marine Renewable Energy Laboratory (MRELab), University of Michigan. The water channel is two-story high and provides a continuous constant flow past the test circular cylinder. 8,000 gallons of water recirculate in the two-story channel moved by an impeller in the lower level, powered by a 20hp induction motor. The test section is 2.44m long and the test cross-section is a rectangular with 1m width and 0.8m depth. To enable flow visualization and measurements with optical instrumentation the test-section walls are made of transparent plexiglass. The length of the cylinder is limited by the width of the LTFSW Channel. Mean velocity distributions were measured at several sections along and across the channel and the maximum flow velocity is about

1.6m/sec. The free stream turbulence intensity is less than 0.1% (Walker et al. 1996). The present study covers the range of Reynolds numbers of $3\times10^4<Re<1.2\times10^5$ where $Re=UD/\nu$ (U=water speed, D=cylinder diameter, ν=water kinetic viscosity). Fig. 2.1 shows the schematic of the LTFSW Channel.

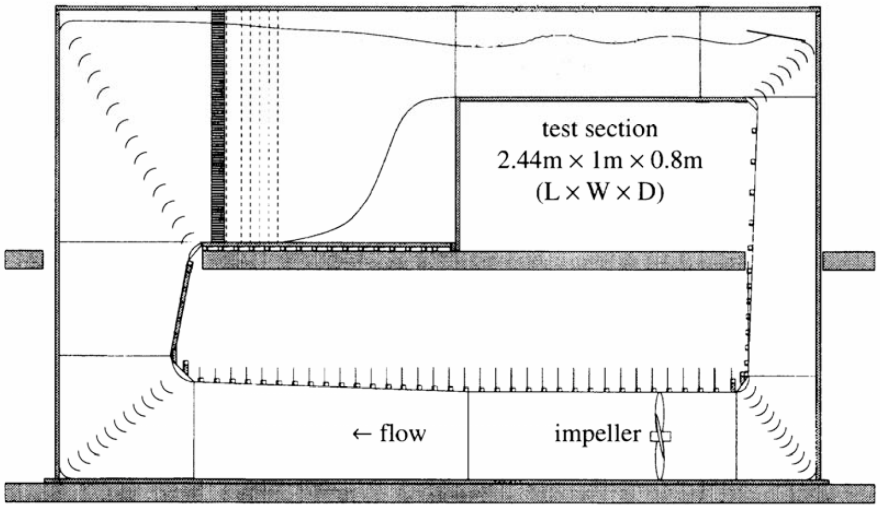

Fig. 2.1. Schematic of the LTFSW Channel [Reproduced from Walker et al. (1996)]

2.2. MOTION MECHANISM

A smooth circular cylinder made of aluminum, with diameter D=0.0889m (=3.5″) and length L=0.914m (=36″) is used for the experiments. To make the cylinder surface smooth and protect it from corrosion, the cylinder was anodized. Allen & Henning (2001) have stated that VIV could be eliminated if the surface is sufficiently smooth. Their observation was made in the transition region where VIV is suppressed anyway. In the present study with a smooth cylinder, significant oscillations are observed with maximum amplitude ratio of about A^*=1.65. In this study, the smoothness of the cylinder surface is

not sufficient to observe the lack of VIV reported by Allen & Henning (2001). The aspect ratio, defined as the length-to-diameter ratio (=L/D), is 10.29. According to Morsbach (1967), for $L/D<<3$, the flow becomes three-dimensional and the separation line of the boundary layer is no longer parallel to the cylinder axis. In the present study and tests, the aspect ratio is much higher than 3 so the flow is assumed to be two-dimensional. The blockage ratio defined as the cylinder diameter divided by the water depth is about 12%.

The test circular cylinder is mounted horizontally suspended by two linear compression coil springs and constrained to move in the transverse direction. The spring is attached by a shaft at each side and the shaft is aligned carefully so that there is no offset or misalignment of the two shafts. Before the tests, the cylinder is placed in the center of the water channel height to minimize the bottom and free surface effects. A gap of 4 cm is maintained between the wall of the LTFSW Channel and the rectangular end-plate of the cylinder. The spring-cylinder system particulars are listed in Table 2.1. Since the end-plates induce effects of their own to the flow around the cylinder, end-plates definitely affect the flow past the circular cylinder. Fox & West (1990) reported that the L/D ratio must be great than 7 to be free from end effects at mid-span. The L/D=10.29 in this study satisfies this requirement and cylinder displacement and visualization are recorded at mid-span. Fig. 2.2 shows a schematic of the motion mechanism. The springs used in the experiments are linear compression springs with a spring constant of about K=763N/m. This spring constant and the damping coefficient were measured by a free-decay test using the logarithmic decrement method. The measurement of these coefficients of the system is presented in Lee (2010) and Chang (2010).

Table 2.1. System particulars

$m_{cylinder}$ (mass of the bare cylinder)	2.535Kg
m (total oscillating mass including 1/3rd of the spring mass)	9.784Kg
m_d (displaced fluid mass) $= \frac{\pi\rho D^2 L}{4}$	5.6707Kg
m_a (added mass) $=C_A m_d$ (C_A=1.0 for a circular cylinder)	5.6707Kg
m^* (mass ratio) $= \frac{m}{\pi\rho D^2 L/4}$	1.725
$f_{N,water}$ (natural frequency in still water)	1.118 Hz
ζ (Damping ratio) $= \frac{c}{2\sqrt{K(m+m_a)}}$	0.0158
K (Spring constant)	763 N/m
C (Damping coefficient)	3.44 Ns/m
ζ (Damping ratio) $= \frac{c}{2\sqrt{Km}}$	0.0199

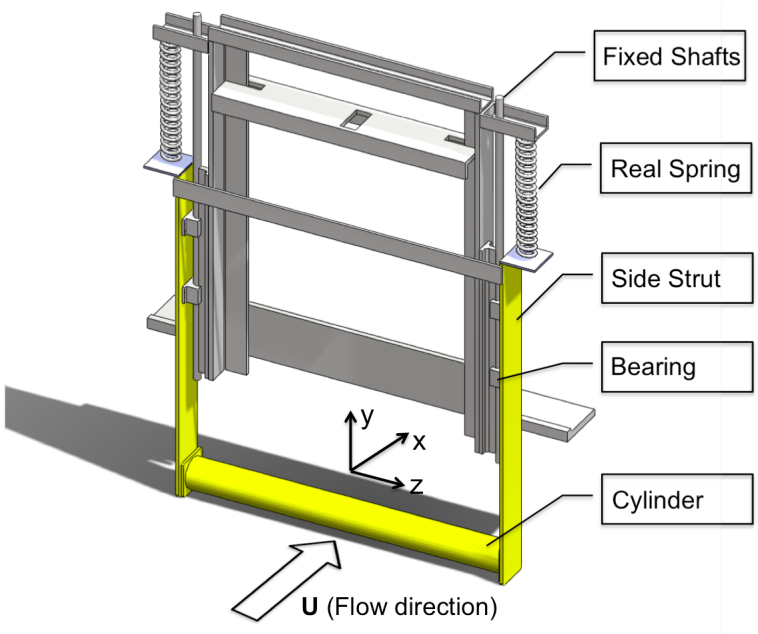

Fig. 2.2. Simple schematic of motion mechanism (real spring system)

For two-cylinder tests in Chapter 9, two new devices have been designed and built and the system particulars such as mass ratio, system damping, and spring constant are

changed. The new devices have less oscillating mass compared to the old device and have different natural frequency in still water. The natural frequency of the two new devices is matched as closely as possible to each other by adjusting the spring constant. The system particulars for the two new devices are listed in Table 2.2.

Table 2.2. System particulars for the new device in 2nd position

	1st position device	2nd position device
$m_{cylinder}$ (mass of the bare cylinder)	2.54 Kg	2.54 Kg
m (total oscillating mass including 1/3rd of the spring mass)	9.53 Kg	9.59 Kg
m_d (displaced fluid mass) $= \frac{\pi\rho D^2 L}{4}$	5.67Kg	5.67Kg
m_a (added mass) $=C_A m_d$ (C_A=1.0 for a circular cylinder)	5.67Kg	5.67Kg
m^* (mass ratio) = $\frac{m}{\pi\rho D^2 L/4}$	1.68	1.69
$f_{N,water}$ (natural frequency in still water)	1.114Hz	1.121 Hz
K (Spring constant)	744.29 N/m	723.38N/m
C (Damping coefficient)	3.46Ns/m	2.67 Ns/m
ζ (Damping ratio) $= \frac{c}{2\sqrt{Km}}$	0.0205	0.016
ζ (Damping ratio) $= \frac{c}{2\sqrt{K(m+m_a)}}$		

2.3. MEASUREMENT AND DATA ACQUISITION

The cylinder oscillatory displacement is measured by a Celesco cable extension position transducer (yo-yo potentiometer). The voltage measurement is done by directly connecting the generator to the data acquisition system in the National Instruments BNC card. The latter consists of a 16-bit analog to digital converter with four-pole, low-pass,

butter-worth filters collecting all the data at a 100Hz sampling rate. Data points are chosen from about every 0.03m/s change of water speed. All the data are recorded for a time interval of 60sec. After changing the speed to the next data point, ample time was allowed to pass before recording new data to avoid transient phenomena. For amplitude plots, the average of the 60 largest positive or negative amplitude values are averaged. In suppression, if 60 peaks are not available 10-20 peaks are averaged; this process overemphasizes the response possibly not showing the full benefits of suppression. Details regarding the calibration of the LTFSW channel are given by Bernitsas et al. 2009.

2.4. VISUALIZATION SETUP

Flow visualization of the near wake on the oscillating circular cylinder is conducted to understand the flow patterns and how they are related to the cylinder response under various flow conditions and PTC configurations. Visualization of flow is made possible by mixing appropriate amount of aluminum oxide particles, 100 micrometer in size, in the re-circulating water. Powder particles are mixed thoroughly with water in a container of suitable size specially made for this purpose. A small, perforated, circular rod, 6mm in diameter dispenser is connected to the bottom of the container. The series of small perforations made in the tube allow the mix to steadily flow out as continuous jets to the main body of water enabling uniform powder deployment in the water covering well the cylinder cross section which is illuminated by a laser sheet. Thus, the flow over the cylinder can be clearly visualized. Fig. 2.3 shows a schematic of the lab visualization.

The laser sheet is projected perpendicularly to the cylinder axis. Laser arrangement used for flow visualization is described in Chang (2010) and Chang et al. (2011).

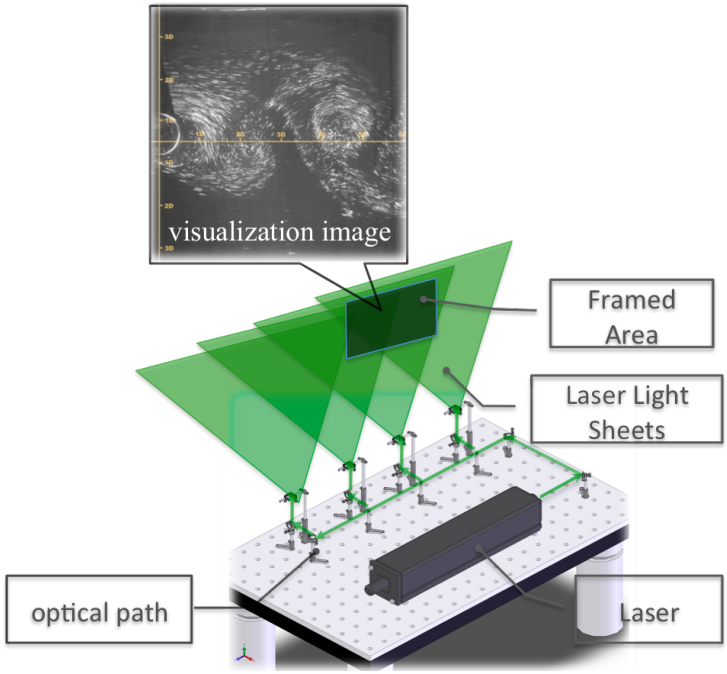

Fig. 2.3. Simple schematic of lab flow visualization

2.5. PASSIVE TURBULENCE CONTROL

Commercially available waterproof sandpaper is used as roughness on the test circular cylinder. The sandpaper is cut into strips of specific width and attached on the surface of the cylinder at specific circumferential locations along the entire length of the cylinder. As aforementioned, roughness is selectively applied on the surface of the cylinder unlike the majority of previous studies where the cylinder surface is completely covered with roughness. The selection of roughness is based on the fact that even small

roughness, on the order of $k/D=10^{-5}$ (k is grit height) influences the flow past a circular cylinder at high Reynolds numbers (Chang & Bernitsas 2011; Chang et al. 2011; Nakamura & Tomonari 1982; Roshko 1970; Szenchyni 1975). Table 2.3 shows the details of roughness applied in the present study.

As seen in Table 2.3, sandpaper consists of paper thickness (H) and roughness height (k) and total thickness (T). T is the sum of paper thickness (H) and roughness height (k). Different strips with roughness designations P60, P120, P180 and a smooth strip are employed for this study. Higher 'P' value corresponds to smoother strip so P60 sandpaper is the roughest sandpaper used in this research. A thin double-sided tape is applied as adhesive medium between PTC (Passive Turbulence Control) and cylinder surface and the adhesive tape has approximate height of 95 micrometer per layer. The smooth strip is a double-sided tape without glue. The total height of the smooth strip is almost the same as the double-sided tape height.

Table 2.3. Roughness size designations

ISO/FEPA Grit designation	Average Particle diameter (μm)	Thickness of backup paper H (μm)	k/D	$(k+H)/D$
P60	269	578	302×10^{-5}	950×10^{-5}
P120	125	528	140×10^{-5}	730×10^{-5}
P180	82	478	92×10^{-5}	630×10^{-5}
Smooth strip	0	95	0	106×10^{-5}

Different configurations are used for the experiments with strip location varied along the cylinder circumference. Results for four kinds of PTC configurations are presented in this thesis. As shown in Fig. 2.4, these designs are designated as straight roughness strips,

inclined sandpaper strips marked as T7, helically applied roughness marked as T6, and staggered roughness strips marked as T8 configurations. For all four configurations, the roughness strips are glued to the cylinder surface symmetrically on both sides of the corresponding ideal-flow front stagnation point.

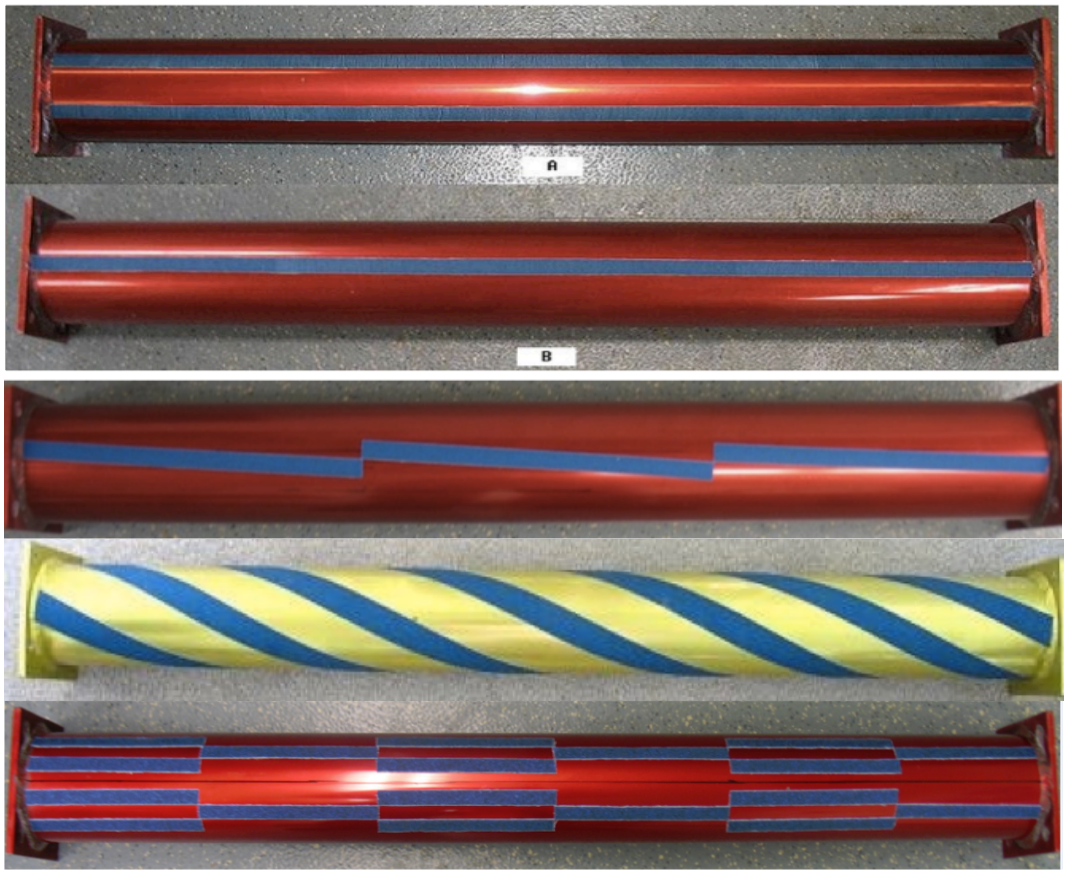

Fig. 2.4. Pictures of PTC configurations. From top to bottom: two straight roughness strips, one straight roughness strip, T7, T6 (helically applied strip), T8 (staggered strip)

As shown in Fig. 2.5, the PTC location is defined by the "placement angle (α_{PTC})", which is the circumferential location of the upstream edge of PTC closer to the front stagnation point and the front stagnation point is considered as 0°. In the results, the coverage is measured from upstream edge to the downstream edge of PTC on the

cylinder surface. For example, 10°-16° means that the upstream edge of PTC is located at ±10° and downstream edge of PTC is located at ±16° from the front stagnation point.

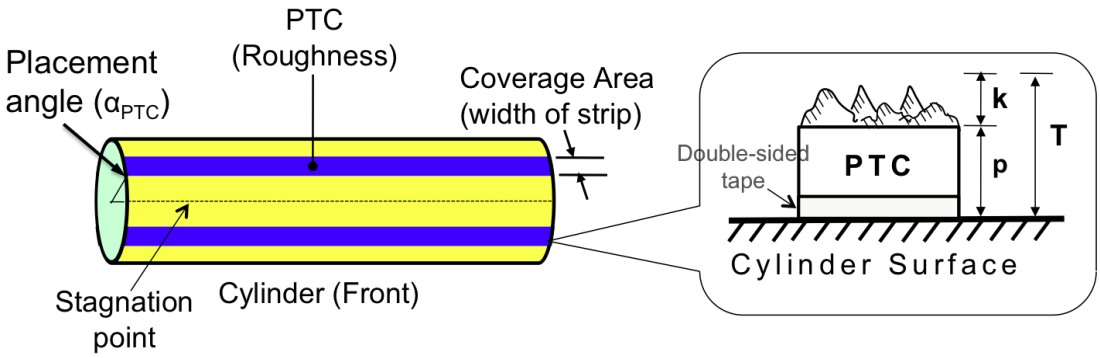

Fig. 2.5. Configuration of roughness strip (PTC) around the cylinder

In Chapter 3, a smooth cylinder response is studied to compare to the response of cylinders with PTC. The smooth cylinder response in the present study is distinctive from those of other researchers because of the high Reynolds number, low mass, and low damping. The results are compared with those of Williamson.

In Chapters 4 and 5, straight roughness strips with half-inch (=1.27cm) and cylinder span length (36″=91.44cm) have been applied with symmetric patterns on various circumferential locations of the circular cylinder to determine the vibratory response characteristics at various flow conditions. But for specific straight roughness configurations with 0°-8° and 172°-180°, only one strip is used instead of two unlike all other cases. For these particular cases, a single strip (width equivalent to 16° approximately) is placed with its mid point coinciding with the stagnation point so that it naturally covers the circumferential angles 0°-±8° and ±172°-±180°, respectively.

In Chapter 6, straight roughness with half (equivalent to 8° approximately) and double (equivalent to 32° approximately) width are applied in the specific response zones found in Chapters 4 and 5. In addition, staggered roughness strips (T8) are introduced to verify the results found in Chapters 4 and 5.

In Chapter 7, six inclined roughness strips (T7) with half-inch width and 12″ (=30.48cm) length are glued on the cylinder surface, symmetrically on both sides from the front stagnation point. The main study is focused on the effect of roughness, location, and roughness strip orientation in suppression.

In Chapter 8, unidirectional and omnidirectional flow suppression PTC are studied. For T8 model, a cylinder is covered by sandpaper strips with a half-inch (=1.27cm) width and 6″ (=15.24cm) length in a staggered pattern. Two different concepts – progressive zone coverage/un-coverage – are used to compare the effect of zones in T8. For progressive zone coverage, the coverage is started from the weak suppression zone WS1 identified in Chapter 6 and a zone is added step by step in each additional experiment. In the final test, the PTC covers all roughness zones. For progressive zone un-coverage, the final roughness configuration from progressive zone coverage is used at the beginning of the test and a zone starting from WS1 is eliminated step by step at each experiment. Finally, the weak suppression zone WS2 is retained in last test. From these experiments, which zone is dominant one or superior to the others is determined. For the T6 configuration, a flow direction independent device, four sandpaper strips with 1″ (=2.54cm) width and 50″ length are wound around a cylinder in the helical strake commonly used in commercial applications for VIV suppression. This design is inspired by helical strakes used in deep water to suppress VIV of tubular structures. Helical

strakes have large height and number of helices and large pitch angle resulting in very high drag increase. On the other hand, the PTC design is cost effective and requires much less coverage and height than helical strakes and it eventually induces less drag. To verify the advantage of selectively applied roughness in FIM, a fully covered roughness cylinder that was tested in previous studies (Güven et al. 1980; Kiu et al. 2011) is also examined for comparison.

In Chapter 9, suppression of two tandem cylinders is studied. Suppression configuration models (T8 and T6) chosen from Chapter 8 are applied to two tandem cylinders and distance between two cylinders center to center is varied from 2.5*D* to 5*D* with 0.5*D* interval. The responses of two smooth cylinders are also shown for comparison.

CHAPTER 3

FIM OF A SINGLE SMOOTH CYLINDER

3.1. LITERATURE REVIEW

3.1.1. Vortex-induced vibrations (VIV)

Vortex-induced vibrations (VIV) is one of the most common fluid induced motions and can be described as a body motion induced by the alternating shedding of von Karman vortices which are produced from the roll up of the shear layers. These body motions can be seen in various cross sectional geometries such as circular, square, and triangular cylinders. When flow passes around a circular cylinder at very broad ranges of Reynolds number, the flow will be slow down and eventually separate at certain angle of the cylinder surface because of viscosity. Then vortices form behind the cylinder changing the pressure distribution along cylinder surface. These pressure distributions cause fluctuating lift and drag forces on the cylinder and on that account the cylinder motion starts for a flexible cylinder or a rigid cylinder on springs. Bishop & Hassan (1963, 1964) directly measured fluctuating drag and lift forces on a stationary and oscillating circular cylinder moving transversely in a direction perpendicular to the flow

direction and their study suggested the existence of a nonlinear fluid-structure interaction oscillator; that is the VIV phenomenon for a cylinder.

As a nonlinear phenomenon, vortex shedding is affected by surface roughness, wall proximity, turbulence intensity, and so on. Achenbach (1968), Achenbach & Heinecke (1981), Farell & Fendeniuk (1988), and Farell & Arroyave (1990) found that even small roughness could change pressure distribution of a circular cylinder so that flow characteristic depending on Reynolds numbers could make an earlier transition in lower Reynolds numbers. When the cylinder is placed near a wall, vortex shedding is suppressed and a stagnation point is moved lower angular position. Consequently, a separation point at the free stream side of the cylinder will move upstream and another separation point at the wall side move downstream. Additionally, incoming turbulence considerably influences the Strouhal number and the effect is similar to the roughness effect, which merges critical, supercritical, and upper transition flow regimes into one transitional region. Beside these topics, VIV on a circular cylinder has been studied for several decades by many researchers on topics such as forces on oscillating cylinders, effect of Reynolds number, mass ratio, damping and so on. Comprehensive reviews on VIV of circular cylinders are discussed in the papers by Sarpkaya (1979, 2004), Williamson & Govardhan (2004), and Gabbai & Benaroya (2005) and the books by Blevins (1990), Sumer & Fredsøe (1997), and Zdrakovich (1997).

In this study, body motion is limited to the cross flow direction. Two-degree flow induced motions are not dealt in this dissertation. When the body is allowed to move both the inline and cross flow directions, dual resonance is observed in cylinder

amplitude response with a 'figure eight' motion. Further study for higher degrees of freedom motions can be found in Jauvtis & Williamson (2004) and Dahl et al. (2010).

3.1.2. Equation of motion

For a rigid bluff body placed normal to a flow of velocity U and mounted on linear springs, the equation of motion for the body can be described by a linear mass-spring dashpot system and modeled by equation (3.1).

$$m\ddot{y} + c\dot{y} + Ky = F_{total}(t) \tag{3.1}$$

where y is the displacement of the body in transverse direction, m is the total oscillating structural mass (i.e. not including added mass), c is a viscous-type damping coefficient of the structure, K is the total stiffness of the springs, and $F_{total}(t)$ is the time-dependent fluid force in the transverse direction.

Equation (3.1) can be rewritten as equation (3.2) using the customary relation of damping coefficient, spring constant, and natural frequency.

$$m\ddot{y} + 2m\zeta\omega_n\dot{y} + m\omega_n^2 y = F_{total}(t) = \frac{1}{2}C_{total}(t)\rho U^2 DL \tag{3.2}$$

where ζ damping ratio, $\omega_n (= \sqrt{\frac{K}{m}})$ the undamped natural frequency of the body in vacuum (absence of fluid effect), and C_{total}(t) instantaneous transverse (lift) force coefficient on the bluff body. Contrary to Bearman (1984) who assumed two-dimensional rigid bluff body so that $C_{total}(t) = F_{total}(t)/(1/2\rho U^2 D)$ and unit of mass is mass per unit span, $C_{total}(t) = F_{total}(t)/(1/2\rho U^2 DL)$ is used as transverse force coefficient in this thesis.

Equation (3.2) is a general equation that explains various FIM in the transverse or in-line directions due to VIV caused by vortex shedding, galloping or turbulence. The transverse coefficient on the right hand side of equation (3.2) accounts for the total instantaneous lift fluid force including fluid inertia and damping forces in the transverse direction acting on a cross section of the oscillating body. Since C_{total} is highly nonlinear and depends on Reynolds number, shape of bluff body, and angle of attack, most of mathematical modeling research of FIM has been aimed at finding a suitable form of C_{total}.

The forces on a moving body consist of two forces - the vortex force due to the vorticity field and the fluid inertia force caused by fluid displacement of the acceleration of the body. For an ideal fluid the fluid inertia force on a circular cylinder is equal to the potential flow (added mass plus pressure gradient) force for a fully submerged cylinder. Hence, the total instantaneous fluid force can be decomposed into a vortex force component and potential force (Wu 1981; Lighthill 1986; Carberry & Sheridan 2001).

Lighthill considered two force components: (a) a force due to the potential flow, which varies linearly with the velocity field and includes the potential added mass force, and (b) a nonlinear, vortex force. The pressure gradient term is not present since the fluid is not accelerating in the y direction. However, his vortex force represents only the force on the body due to the additional vorticity: the vorticity field minus the distribution required to generate the potential flow slip boundary condition at the body.

$$F_{total} = -\rho \frac{d}{dt} \int_{Vc} \vec{r} \times \vec{\omega} + \rho \frac{d}{dt} \int_{Vb} \vec{u}\, dV$$

$$= F_{vortex} + F_{potential} \qquad (3.3)$$

where V_c is a distant external boundary containing all the shed vorticity and V_b is the

volume bounding the solid body.

The instantaneous potential added-mass force acting on the cylinder is given by

$$F_{potential} = -C_A m_d \ddot{y}(t) \tag{3.4}$$

where C_A is the potential added mass coefficient and m_d is the displaced fluid mass.

By normalizing equations (3.3) and (3.4) by $\frac{1}{2}\rho U^2 DL$ and substituting $y = A\sin(\omega t)$ into equation (3.4), we get two equations

$$C_{total}(t) = C_{vortex}(t) + C_{potential}(t) \tag{3.5}$$

$$C_{potential}(t) = 2\pi^3 \frac{y(t)/D}{(U^*/f^*)^2} \tag{3.6}$$

Vortex force can be computed by using equations (3.3-3.6). As seen in equations (3.4) and (3.6), the instantaneous potential added-mass force is always in-phase with the cylinder motion *y(t)*. There is discrepancy on treating the added mass term. Blevins (1990) and Sumer & Fredsøe (1997) put the added mass on the left hand side of the equation of motion and added mass term is absorbed into the total oscillating mass while Bearman (1984) left the added mass term on the right hand side of the equation of motion. However, the fluid force can be described as the 'lift force', regardless of including or excluding the added mass term. In order to understand the loading caused by the complex mechanism of vortex shedding, it is more instructive to avoid this controversy in this dissertation so that all fluid forces are placed on the right hand side of equation (3.2) unless stated otherwise.

For large amplitude VIV, where the body oscillation frequency is synchronized with the vortex shedding frequency, it is assumed that the structure has a constant amplitude

and harmonic response. Furthermore, the transverse force due to vortex shedding drives the oscillator system with the same frequency f_{osc} and a phase angle ϕ_{total} from displacement response. Hence, the displacement *y(t)* and the fluid force *F(t)* can be approximated by the equations (3.7) and (3.8)

$$y = A\sin(\omega t) = A\sin(2\pi f_{osc} t) \tag{3.7}$$

where A is the maximum value of the transverse displacement and f_{osc} is the frequency of oscillation observed in the experiments

$$F_{total}(t) = F_{\max}\sin(\omega t + \phi_{total}) = \frac{1}{2}\overline{C_{total}}\rho U^2 DL\sin(\omega t + \phi_{total})$$
$$= \frac{1}{2}\overline{C_{total}}\rho U^2 DL\sin(2\pi f_{osc} t + \phi_{total}) \tag{3.8}$$

where the maximum force is given by $F_{\max} = 1/2\overline{C_{total}}\rho DLU^2$.

By substitution of these approximations into equation (3.2) and collecting sine and cosine terms, the following equations are derived.

$$\frac{\overline{C_{total}}\rho DLU^2}{8\pi^2 Am(f_N)^2}\cos\phi_{total} = \left[1 - \left(\frac{f_{osc}}{f_N}\right)^2\right] \tag{3.9}$$

$$\frac{A}{D} = \frac{\overline{C_{total}}L}{4\pi^2}\sin\phi_{total}\left(\frac{\rho D^2}{2m\zeta}\right)\left(\frac{U}{f_N D}\right)^2\frac{f_N}{f_{osc}} \tag{3.10}$$

Equation (3.9) can be rewritten as equation (3.11)

$$\frac{f_{osc}}{f_N} = \left[1 - \frac{\overline{C_{total}}L}{4\pi^2}\cos\phi_{total}\left(\frac{\rho D^2}{2m\zeta}\right)\left(\frac{U}{f_N D}\right)\left(\frac{y}{D}\right)^{-1}\right]^{1/2} \tag{3.11}$$

Hence, the amplitude ratio *A/D* is represented by equation (3.10) and the ratio of the oscillation frequency to the natural frequency is derive by equation (3.11).

When a bluff body oscillates at large amplitude in air, the mass parameter $\rho D^2/2m$,

which is proportional to the inverse of m^*, in equation (3.11) might be typically of order 10^{-3}. Hence, the frequency of body oscillations is close to its natural frequency and the steady state response amplitude of a bluff body to vortex shedding can be replaced by equation (3.12)

$$\frac{A}{D} = \frac{\overline{C_{total}}L}{4\pi^2}\sin\phi_{total}\left(\frac{\rho D^2}{2m\zeta}\right)\left(\frac{U}{f_N D}\right)^2 \tag{3.12}$$

On the other hand, when a structure is exposed to a denser fluid such as water, $\rho D^2 / 2m$ may be on order of unity and the frequency of oscillation of the body can be substantially different from its natural frequency and vary with reduced velocity. This frequency ratio difference depending on the fluid is proved by experiments.

From equation (3.12), it is clear why suppressing VIV is more difficult in water than in air. The amplitude ratio in equation (3.12) is influenced by the inverse of the combined mass-damping parameter ($2m\zeta / \rho D^2$). This parameter is referred to as the Scruton number in wind and offshore engineering. The Scruton number is a significant parameter in vortex excitation, rain/wind-induced vibration, galloping of cable, wake galloping for group of cables, and dry inclined cable galloping. By increasing the Scruton number (increasing mass and damping of the structure), FIM can be alleviated. Since VIV has a much smaller mass-damping parameter value in water than in air, it is more difficult to suppress VIV in water compared to air.

The phase angle ϕ_{total} plays an extremely important role in equations (3.10) and (3.11). The response amplitude depends not only on C_{total} but also on that part of C_{total} in phase with the body velocity. Hence, measurements of the sectional fluctuating transverse force coefficients on a range of stationary bluff body shapes will give little

indication of the likely amplitudes of motion of similar bodies flexibly mounted.

3.1.3. Effect of mass ratio and synchronization

For stationary cylinders, the vortex shedding frequency is related to the Strouhal number which is defined as $St=f_vD/U$. The Strouhal number is found to be nearly constant with a value of 0.2 for a large range of Reynolds numbers. On the other hand, oscillating cylinders have a distinctive feature called synchronization or lock-in phenomenon. At low flow speed, the vortex-shedding frequency follows the Strouhal number relation. But as flow speed increases, the shedding frequency deviates from the Strouhal number relation and starts to follow the frequency of oscillation f_{osc} (locked-in to f_{osc}). At resonance, where high amplitude oscillation is occurred, mass ratio has significant influence on the amplitude and frequency response. Fig. 3.1 shows the difference of VIV response in air and water where air has higher mass ratio than water. Feng (1968) conducted VIV tests in air and the mass ratio was 248 while Khalak & Williamson (1999) conducted VIV tests in water and the mass ratio was 10.1. For the high $m^*\zeta$ experiments of Feng (1968), there exist two branches separated (initial and lower) with one discontinuous mode transition. In the initial branch, the highest amplitudes are observed, and the amplitude decreased sharply in the lower branch, with a hysteresis between the two branches. On the other hand, the low $m^*\zeta$ experiments of Khalak & Williamson (1999) have three distinct branches – initial, upper, and lower branches – with two mode transition. The synchronization range is broader and the highest amplitude in the upper branch is much higher than Feng (1968)'s experiments.

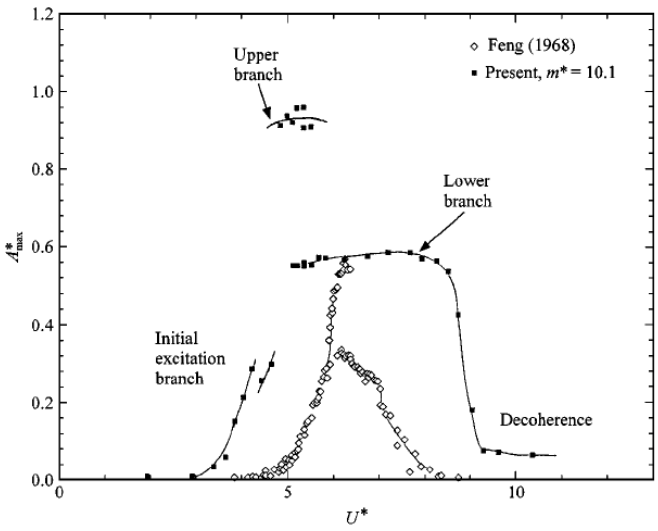

Fig. 3.1. Amplitude response plot for high and low $m^*\zeta$ (Khalak & Williamson 1999)

The classic meaning of 'lock-in' or 'synchronization' phenomenon (Sumer & Fredsøe 1997) is that as the fluid velocity is increased, the vortex-shedding frequency f_v approaches the natural frequency of the structure in still water $f_{N,w}$ and the two frequencies synchronize at certain flow speed. Further increase of U^*, the shedding frequency deviates from the Strouhal frequency (stationary cylinder) and the shedding frequency and the oscillation frequency f_{osc} become close to $f_{N,w}$. Hence, the frequency ratio $f^*=f_{osc}/f_{N,\mathrm{w}}$ remains close to unity over the synchronization range. Since the frequency ratio departs from unit at low mass ratio, this definition of synchronization is not valid for low mass ratio and a new definition is needed.

Khalak & Williamson (1999) suggested that the 'synchronization' term mean the matching of the frequency of the periodic wake vortex mode with the body oscillation frequency. As seen in Fig. 3.3, for large mass ratios such as in air VIV, when large cylinder motion at resonance, the cylinder oscillation frequency f_{osc} will be close to the vortex-shedding frequency for the static cylinder f_v, (Strouhal frequency) and also close

to the system natural frequency $f_{N,w}$. Therefore all three frequencies are close to each other ($f_{osc} \approx f_v \approx f_{N,w}$) and the frequency ratio is close to unit ($f^* \approx 1.0$) as proven by equation (3.11). From these relations, Bearman (1984) showed that the onset of resonance in terms of U^* is at:

$$\frac{U^*}{f^*} = \frac{U/(f_{N,w}D)}{f_{osc}/f_{N,w}} = \frac{U}{f_{osc}D} \approx \frac{U}{f_v D} = \frac{1}{St} \tag{3.13}$$

where St is the Strouhal number of the static cylinder and has a value of 0.2-0.21. By equation (3.13), the resonance occurs at the $U^* \approx 5\text{-}6$.

However, for low mass ratio such as water, the frequency ratio f^* is not unity as verified by equation (3.11) and increases up to 1.4 over the synchronization range $U^* = 4\text{-}11$ as seen in Fig. 3.2. This departure from unity is due to the effect of the added mass coefficient (Sarpkaya 1978). Nondimensional f^* definition introduced by Khalak &Williamson (1999) can be obtained from equation (3.2) by moving the added mass term to the left hand side of the equation of motion.

$$f^* = \sqrt{\frac{m^* + C_A}{m^* + C_{EA}}} \tag{3.14}$$

where C_{EA} is effective added mass coefficient ($= \frac{1}{2\pi^3} \frac{C_{total} \cos\phi_{total}}{A^*} \left(\frac{U^*}{f^*} \right)^2$) and C_A is the theoretical added mass coefficient ($C_A = 1$).

From equation (3.14), when the mass ratio m^* becomes smaller, the effective added mass coefficient C_{EA} plays significant role in the frequency ratio f^* and the departure from unit would be expected. Moe & Wu (1990), Khalak &Williamson (1997b) and Gharib et al. (1998) reported experimentally the departure of f^* from unity through the synchronization regime.

It is worthy to note that the shedding frequency does not necessarily match the oscillation frequency over the synchronization range, because the wake mode might include more than two vortices per cylinder cycle. Thus, Khalak &Williamson (1999) instead of using a synchronization definition which matches the shedding frequency to the body oscillation frequency, suggested using a different definition. Specifically, as the match of the frequency of the periodic wake vortex mode (f_w) to the body oscillation frequency (f_{osc}). Correspondingly, the transverse force frequency must match the body oscillation frequency.

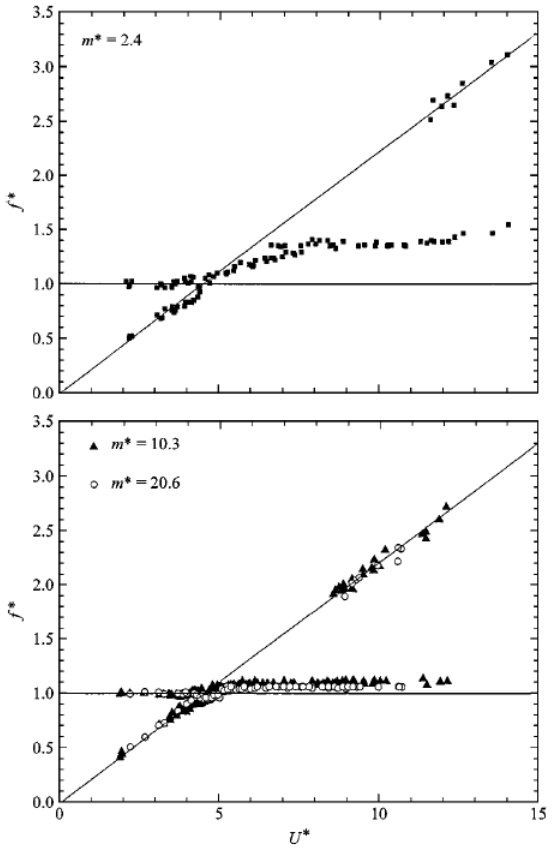

Fig. 3.2. Frequency response for a range of mass ratios, m^*, through the synchronization regime (Khalak & Williamson 1999)

3.1.4. Phase jump

As shown in equations (3.7) and (3.8), there exists a phase difference between the cylinder displacement and the transverse (lift) force. This phase difference has significant influence on the cylinder amplitude as already seen in equation (3.12). Bishop & Hassan (1963) found that the lift force undergoes a sharp change in amplitude and phase over the synchronization regime. Then Zdravkovich (1982) explained first that this sharp change of the phase angle corresponds to a switch of vortex shedding timing relative to the body motion. Later, this fact was confirmed by experiments (Gu et al. 1994) and numerical simulations (Meneghini & Bearman 1995; Lu & Dalton 1996).

By forced oscillation experiments of broad range of flow speed U^* and amplitude A^*, Williamson & Roshko (1988) found various vortex formation modes associated with specific regions such as 2 single vortices (2S), 2 pairs of vortices (2P), or three vortices (P+S) per cycle (Fig. 3.4). Further Williamson & Roshko found that the initial branch of Feng (1968) is associated with the 2S mode and the lower branch with the 2P mode. Govardhan & Williamson (2000) who used DPIV (Digital Particle Image Velocimetry) measurements for the first time in free vibration verified these vortex formation modes. Further Hover et al. (1998) who used a virtual m-c-k system, based on a different approach form the one developed in the MRE lab in University of Micghian (Lee et al, 2010), to produce free vibration also confirmed that the initial branch shedding is of the 2S mode, and the lower branch is of the 2P mode. Blackburn & Henderson (1999) proposed that two different mechanisms of vorticity production compete each other and this competition is reason for this switch of timing. Carberry et al. (2001) who used

forced oscillation showed that changes in the lift force are associated with the changes in the near-wake structure and the changes in the vortex shedding mode is connected to the change of vortex formation timing. As a result, the changes in the vortex shedding mode is related to the phase shift of the lift force.

It is a well-known fact that at high $m^*\zeta$, phase angle jumps during the transition between initial and lower branches. From Khalak & Williamson (1999) experiments of the low $m^*\zeta$ case, two-mode transitions are observed between initial and upper branch with hysteresis and between upper and lower transition with intermittent switching as shown in Fig. 3.4.

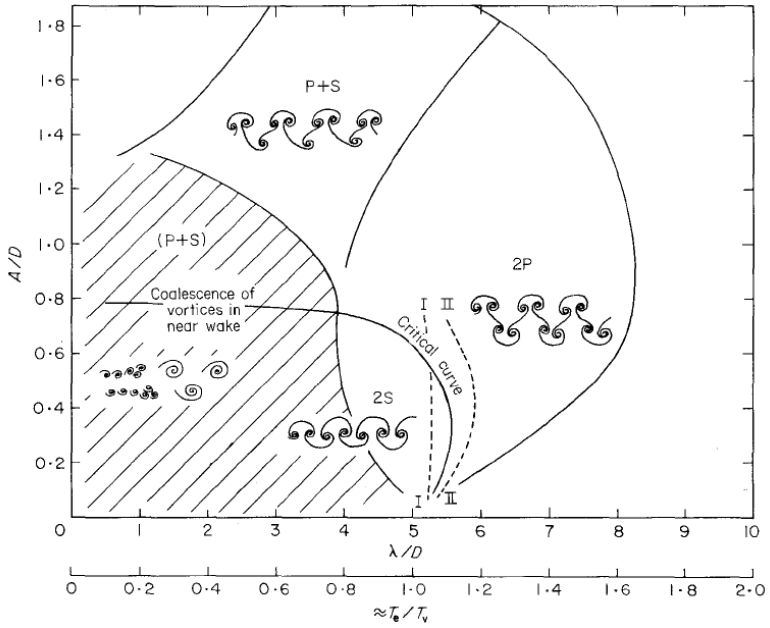

Fig. 3.3. Map of vortex synchronization pattern (Williamson & Roshko 1988)

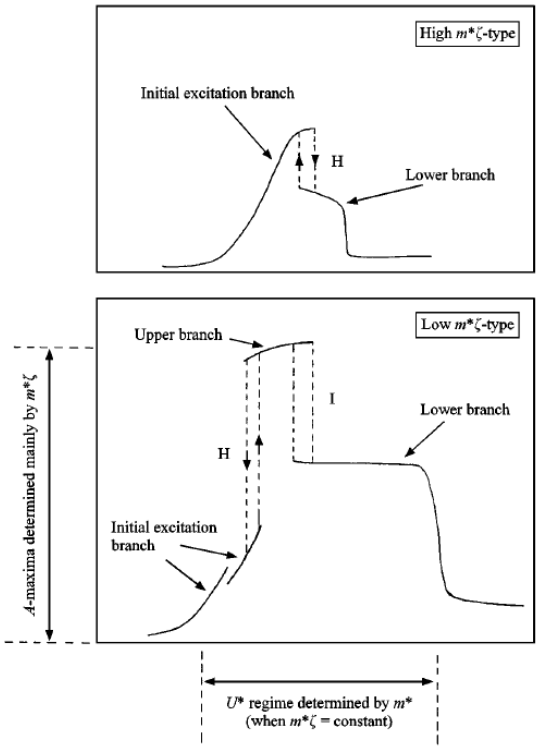

Fig. 3.4. Two distinct types of amplitude response are shown here schematically (Khalak & Williamson 1999)

The mode transition in a low $m^*\zeta$ case can be explained by the mathematical model introduced in Section 3.1.2. Since the total transverse force can be decomposed into potential force and vortex force, the equation of motion can be rewritten using the vortex force term. By substituting equations (3.2) and (3.3) and assuming sinusoidal excitation, equation (3.1) can be modified as

$$(m+m_A)\ddot{y}+c\dot{y}+Ky=F_{vortex}(t)=F_{vortex}\sin(\omega t+\phi_{vortex}) \tag{3.15}$$

where ϕ_{vortex} is phase between vortex force and displacement.

Plugging equation (3.7) into equation (3.15) and collecting sin term, we find

$$\frac{F_{vortex}\cos\phi_{vortex}}{KA}=1-\left(\frac{f_{osc}}{f_{N,w}}\right)^2 \tag{3.16}$$

From the equation (3.16), ϕ_{vortex} jumps through 90° when $f_{osc}/f_{N,w}$ passes through unity. The mode change of initial (2S mode) to upper (2P mode) branch is associated with a jump in vortex phase ϕ_{vortex} as the response frequency passes through $f_{osc}/f_{N,w}$=1. Since the vortex force is associated with vortex formation and the convection of shed vorticity (Lighthill 1986), the phase jump of vortex force always relates to change in vortex shedding timing.

Similar to the mode change from the initial to the upper branch, ϕ_{total} jumps through 90° when $f_{osc}/f_{N,w}$ passes through unity. The transition of upper (2P mode) to lower (2P mode) branch is related to a jump in phase ϕ_{total} as the response frequency passes through f_{osc}/f_N =1. It is worthy to note that contrary to Zdravkovich (1982)'s observation, where phase jump is related to a change of vortex shedding timing, this phase ϕ_{total} jump is not always related to a switch of the vortex shedding timing (Govardhan & Williamson 2000). Fig. 3.5 shows a summary of phase jumps between the three response branches.

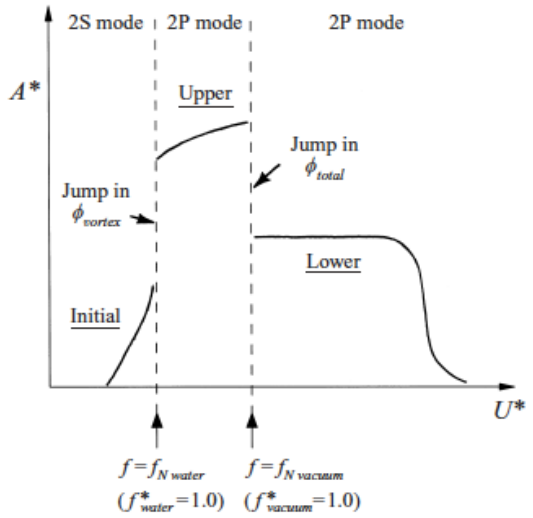

Fig. 3.5. Schematic diagram of the low ($m^*\zeta$) type of response showing the three principal branches (initial, upper and lower), and correspondingly the two jump phenomena (Govardhan & Williamson 2000)

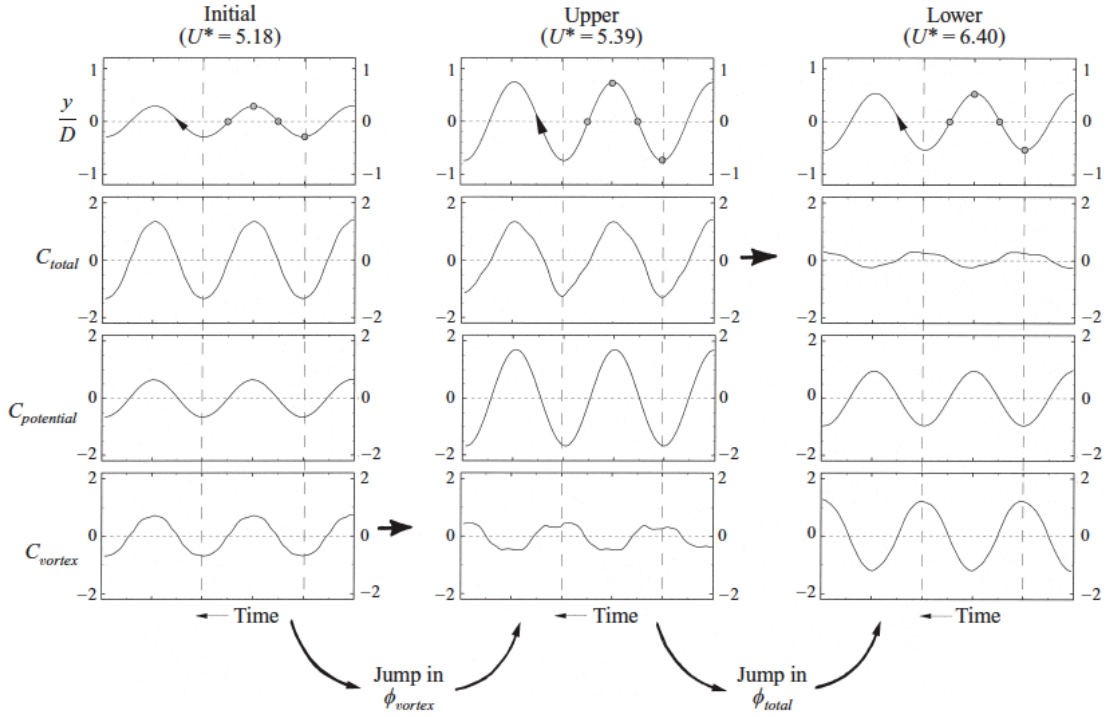

Fig. 3.6. Relationship between total transverse force coefficient (C_{total}), the potential added mass force coefficient ($C_{potential}$) and the vortex force coefficient (C_{vortex}) in the three response branches. Low ($m^*\zeta$) (m^*=8.63, ζ=0.00151) (Govardhan & Williamson 2000)

As seen in Fig. 3.6, the total force coefficient has a large value at the initial branch since the potential and vortex forces are in phase. At the upper branch, the total force maintains large value. The potential force is sufficiently increased but the vortex force undergoes a phase jump and goes out of phase (phase change of roughly 180°). At the lower branch, the total force undergoes a phase change of roughly 180°. The reason is that the dramatically increased vortex force cancels out the slightly decreased potential force coefficient. Thus, the total force has the same phase as the vortex force.

3.1.5. Drag and lift coefficients for oscillating cylinder

When a stationary cylinder is exposed to a steady flow, vortex shedding creates oscillating forces on the circular cylinder. As the vortex shedding alternates, the force and the pressure distribution around the cylinder change periodically. The vortex shedding at the lower edge of the cylinder gives upward lift force whereas the vortex shedding at the upper edge of the cylinder gives downward lift force. Both vortices at the upper and lower edge of the cylinder give a temporary increase in the drag. It is a well known fact that the frequency of the lift force is the same as the wake vortex mode frequency, f_w, while that of the drag force is twice the vortex-shedding frequency. Gerrard (1961), Achenbach (1968), and Ribeiro (1992) found the fluctuating force of the stationary cylinder by pressure integration. Unlike them, Bishop & Hassan (1963) directly measured lift, fluctuating drag, and drag forces on a stationary cylinder and found that the three forces are all strongly connected to each other and a change in one will necessarily change the other two.

For an oscillating circular cylinder moving transversely in a direction perpendicular to the flow direction, Bishop & Hassan (1964) showed that lift coefficient for oscillatory cylinder is considerably large compared to that of an oscillating one. Mercier (1973) and Sarpkaya (1995) found that the mean drag of an oscillating cylinder is up to 3.5 times that of stationary cylinder. Later Khalak & Williamson (1999) measured forces on a circular cylinder at low mass ratio (m^*=3.3) and found that the fluctuating lift and mean drag coefficients are seven and five times higher than those of the stationary cylinder, respectively. Surprisingly, the fluctuating drag coefficient is 102 times higher than that of the stationary cylinder.

3.2. RESULTS, OBSERVATIONS, AND DISCUSSION

In all amplitude and frequency response figures for cylinders with PTC presented in this thesis, the corresponding smooth cylinder results are plotted for comparison. Results are plotted vs. Reynolds number (Re), reduced velocity (U^*), and actual water velocity. The definition of the natural frequency in water (see Nomenclature) is disputed as being non-constant and depending on added mass, which varies with U^* (Sarpkaya 1979; Vikestad et al. 2000). In this thesis, the reduced velocity used is defined by the natural frequency in still water using the ideal added mass. This affects the presentation of results but not their validity.

Amplitude and frequency response for a smooth cylinder are discussed in Section 3.2.1. Displacement time history and power spectrum are discussed in Section 3.2.2. These results are used for comparison with PTC cylinders. Approximately calculated lift coefficient and phase angle are discussed in Section 3.2.3. Near-wake structures of the smooth cylinder are also discussed Section 3.2.4.

3.2.1. Amplitude and frequency response

Fig. 3.7 shows amplitude and frequency response of a smooth cylinder. The smooth cylinder response in this study is accomplished under low mass ratio and low mass damping and the response is distinctive from Feng (1968). Feng conducted his investigation in air and as a result the mass ratio was much higher than a test in water. Feng's smooth cylinder response had two amplitude branches namely the initial and

lower branches. Unlike high mass ratio, low mass ratio with low damping response is characterized by three distinct branches: the initial, upper and lower branches. Our smooth cylinder response also has the initial branch ($4<U^*<5.5$), upper branch ($5.5<U^*<10.8$), and lower branch ($10.8<U^*<12.2$) ending in de-synchronization ($U^*>12.2$). These results generally agree with observations in previous studies of a circular cylinder at low mass ratio (Khalak & Williamson 1996, 1997a,b, 1999; Blevins & Coughran 2009). Since this study is achieved at higher Reynolds number than those of Khalak& Williamson (1996, 1997a,b, 1999), there are differences in the VIV response in this study from previous study. As shown in Fig. 3.7, the smooth cylinder amplitude in the upper branch varies with respect to reduced velocity almost linearly. Blevin & Coughran (2009) also observed this feature, contrary to the nearly constant slightly curve-linear profile reported by Khalak & Williamson (1999). Also the upper branch in this thesis is much broader ($5.5<U^*<10.8$) with high amplitude occupying most of the VIV synchronization regime than that of Khalak & Williamson (1999) ($4.7<U^*<6$). The reason for this is mass ratio and the high Reynolds number. According to Khalak & Williamson (1999), the width of the synchronization regime is governed by the mass ratio. The mass ratio in the present study is 1.84 and Khalak & Williamson (1999) study was 10.1. When Khalak & Williamson (1999) used mass ratio of 2.4, the overall VIV range including the initial, upper and lower branches covered $3<U^*<11.2$ and is close to the present study. The maximum amplitude of the smooth cylinder in the upper branch is $1.6A^*$ and is generally higher than that of any other researchers. The reason is the high Reynolds numbers influence (Bernitsas et al. 2006a,b; Bernitsas & Rakhavan 2007, 2008, 2009, 2011; Chang & Bernitsas 2011; Chang et al. 2011; Kim et al. 2011; Lee &

Bernitsas 2011; Lee et al. 2011; Park et al. 2011; Raghavan & Bernitsas 2007a,b, 2011; Wu et al. 2011). The Reynolds number regime of the current study is in TrSL3 flow regime and has higher fluctuating lift coefficient than any other regime (Zdravkovich 1997). This high fluctuating lift coefficient influences the maximum peak and the whole VIV region. In addition to that, the lower branch is short ($10.8<U^*<12.2$) and its amplitude decreases steadily in contrast to the nearly flat and broader range ($5<U^*<9$ for $m^*=10.3$ and $5<U^*<11$ for $m^*=2.4$) of that of Khalak & Williamson (1999). It is interesting to note that present study does not show noticeable two mode transitions - one with hysteresis between the initial and upper branch and another with an intermittent switching of modes between upper and lower branch. These transitions may be caused at very short reduced velocity and current test setup is not available to alter reduced velocity sensitive enough to catch the transitions.

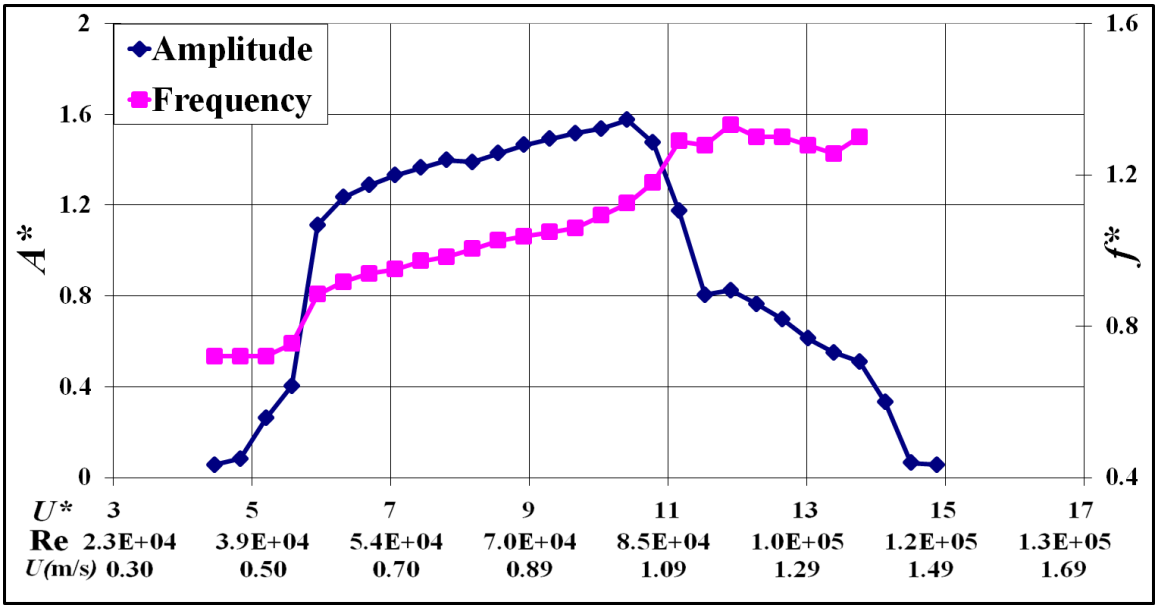

Fig. 3.7. Amplitude and frequency response of smooth circular cylinder

In this dissertation, the frequency ratio (f^*) is defined as the ratio of the body

oscillation frequency (f_{osc}) to the fixed natural frequency of the system ($f_{N,w}$) in still water differently from Sarpkaya (1995) who defined the natural frequency ($f_{N,w}$) same as to f_{osc}, to match frequency ratio f^* to unit over the synchronization range. As seen in Fig. 3.7, at the initial branch the smooth cylinder, the frequency ratio increases from 0.62 at $U^* \cong 4$ to 0.82 at $U^* \cong 5.5$ and a jump is observed at $U^* \cong 5$. After $U^* > 5.5$, the frequency ratio increases steadily up to at the end of the lower branch and reaches about 1.3 at $U^* \cong 12.2$. Contrary to large mass ratio, which had frequency ratio near unit, frequency ratio at low mass departs from unity and this departure agrees with the observations of previous investigators (Moe & Wu 1990; Khalak & Williamson, 1997b). This deviation of frequency ratio from unity is attributed to the expected influence of an effective added mass coefficient and the effective added mass coefficient increases as the mass ratio becomes smaller. It is worthy of note that frequency ratio is not constant at the lower branch contrasted to Govardhan & Williamson (2000) reporting constant level of frequency ratio in low mass damping and introducing the possibility of a critical mass ratio. Since the Reynolds number in the lower branch is close to the critical region, the lower branch region is short and the frequency ratio could not develop fully to constant level. At de-synchronization, the dominant frequency of the oscillation disappears because VIV is dependent on Reynolds numbers (Raghavan & Bernitsas 2007a,b) and VIV is suppressed at high Reynolds numbers whereas other researchers (Khalak & Williamson 1996; Govardhan & Williamson 2000) could measure frequency ratio in de-synchronization.

3.2.2. Displacement and power spectrum

At the beginning of the initial branch, U^*=4.84, the displacement time history in Fig. 3.8(a) shows quasi-periodic oscillations. The corresponding spectrum shows a major peak at the body oscillation frequency f_{osc}=0.806Hz (f^*=0.721) and two minor peaks, one at the Strouhal frequency (vortex shedding frequency of the stationary cylinder) f_s=1.082Hz and the second one at the natural frequency of the cylinder in water $f_{n,w}$=1.118Hz. At m^*=2.4, Khalak & Williamson (1996) also have observed similar amplitude quasi-periodic wave forms in the initial branch. When the reduced velocity is increased to U^*=5.6 in the initial branch, response is marked with much better periodicity as shown in Fig. 3.8(b). The corresponding frequency spectrum shows only one predominant spike at the oscillation frequency f_{osc}=0.84Hz (f^*=0.753). Oscillations still exhibit certain degree of modulation. However, results at still higher m^*=8.63 show much more stable and steady amplitudes in the initial branch (Fig. 4 of Govardhan & Williamson 2000). When U^* is further increased to U^*=8.56 in the upper branch (Fig. 3.8(c)), variation in amplitude is further decreased and cylinder oscillations are steady and periodic. The frequency spectrum shows additional spikes at $2f_{osc}$ and $3f_{osc}$ as shown in Fig. 3.8(c). In the upper branch at m^*=2.4, Khalak & Williamson (1996) observed notable amplitude modulations in their Figs. 11(a)-(ii). At U^*=10.42 in Fig. 3.8(d) near the end of the upper branch, cylinder oscillations become more non-uniform but with frequency characteristics similar to those at U^*=8.56. The increased amplitude modulations observed are attributed to the intermittent switching of amplitude between the upper and the lower branches (Khalak & Williamson 1999). In the lower branch at U^*=12.65 in Fig. 3.8(e), the vibrations are not steady exhibiting greater modulations in contrast to the

nearly steady oscillations reported by Khalak & Williamson (1996). Further in the lower branch, at a still higher U^*=13.40, exceedingly higher modulations are observed in Fig. 3.8(f). The corresponding frequency spectra also show a more or less uniformly distributed pattern similar to what is usually expected in the desynchronization. In the lower branch in Fig. 2, amplitude decreases steadily in contrast to the nearly flat and broader profile observed by Khalak & Williamson (1999). At U^*=14.89 (desynchronization), only feeble oscillations are observed as shown in Fig. 3.8(g). The corresponding spectrum is nearly uniformly distributed with no predominant wake frequencies. Further, the remarkable similarity is seen between the amplitude wave forms at U^*=12.65 (Fig. 3.8(e)) and the beating phenomenon reported (Fathi, 2009) in the vibratory wave form of a cylindrical roller bearing (Fig. 3.9).

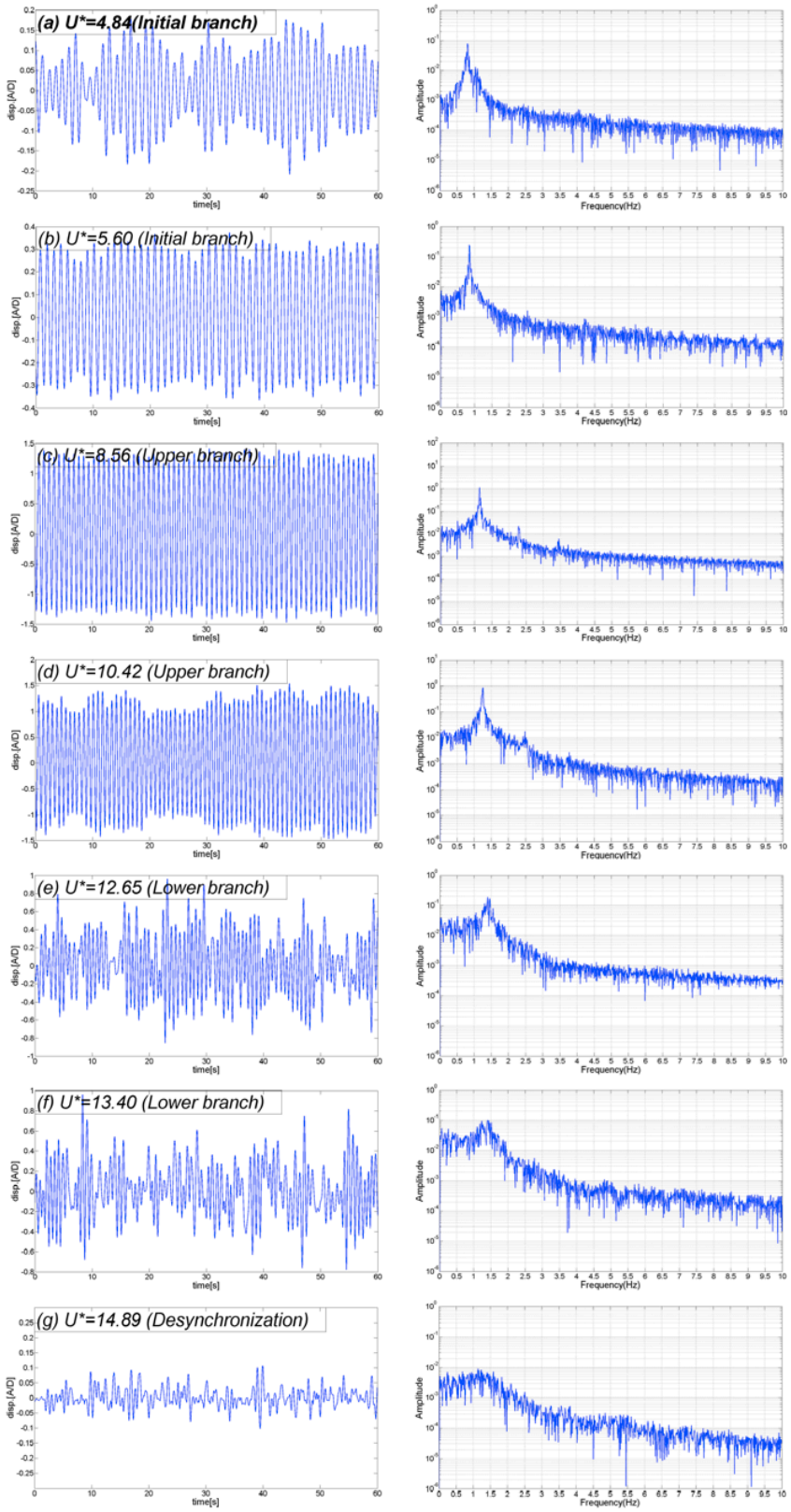

Fig. 3.8. Smooth cylinder displacement: time series and frequency spectra

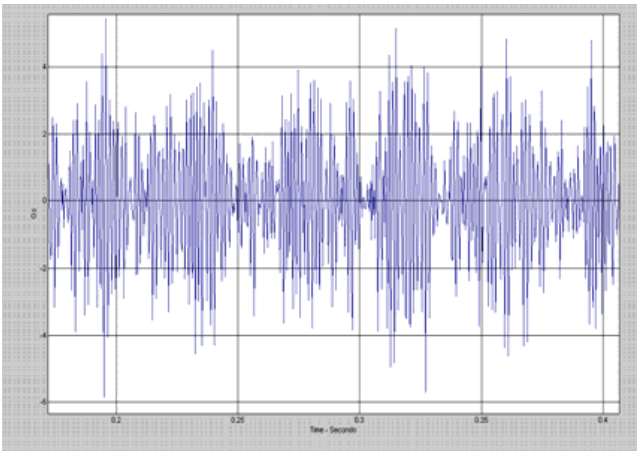

Fig. 3.9. Beating phenomenon in the vibratory wave form of a cylindrical roller bearing (Fathi 2009)

3.2.3. Calculation of C_{total}, C_{vortex}, ϕ_{total} and ϕ_{vortex}

The transverse force coefficients (C_{total}, and C_{vortex}) and the phase angles (ϕ_{total} and ϕ_{vortex}) between the fluid force and the cylinder displacement are calculated for a broad range of reduced velocity covering the initial branch, the upper branch and the lower branch. To calculate the fluid force, velocity and acceleration of the cylinder is calculated by directly differentiating displacement time histories. Because of noise in the displacement signal, a filter is applied. Filtering usually causes phase lag compared to the original signal. Hence, filtering is used two times to remove the phase lag. The first filter removes the noise in the displacement signal and the second filter removes the phase lag between original and filtered signal. Fig. 3.10 shows one example of a filtered displacement signal where the phase lag between the original and filtered signal was eliminated. As seen in Fig. 3.11, filtering noise in the displacement signal is crucial particularly in the acceleration history where the displacement signal was differentiated

twice. The acceleration of the filtered displacement signal shows a much cleaner signal than that of the original displacement signal.

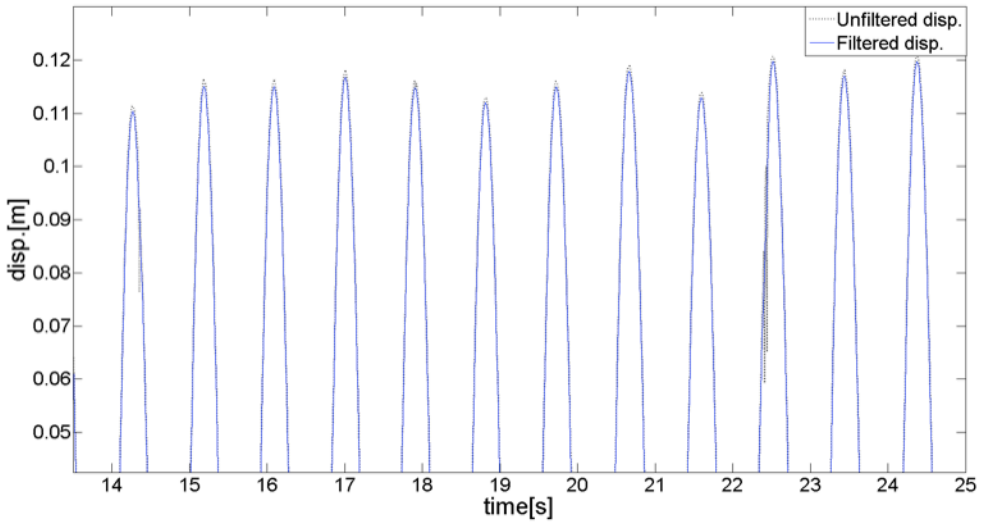

Fig. 3.10. Comparison between unfiltered and filtered displacement

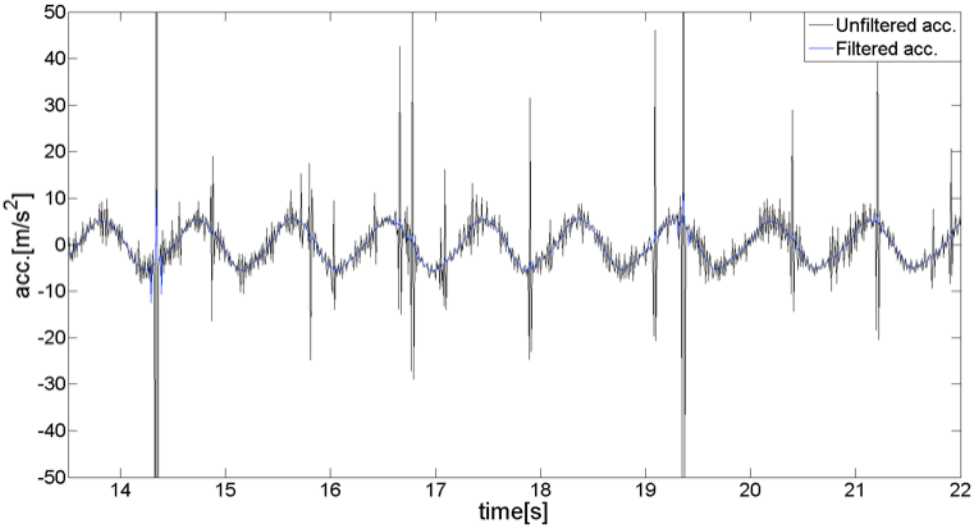

Fig. 3.11. Comparison between unfiltered and filtered acceleration

The transverse force coefficients (C_{total}, and C_{vortex}) and the phase angle (ϕ_{total} and ϕ_{vortex}) are calculated by inverse dynamics. From the equation of motion (equations 3.1 and 3.15), all the values are known except for the transverse force. Time histories of transverse forces can be found by processing displacement, velocity, and acceleration signals.

Figs. 3.12-3.14 show time histories of displacement, C_{total}, $C_{potential}$, and C_{vortex} calculated at the initial, upper and lower branches. Fig. 3.12 shows time histories of all four signals in the initial branch at U^*=5.58 and all four signals are nearly in phase. As the reduced velocity increases, ϕ_{vortex} jumped and only the vortex force is out of phase with the others in the upper branch at U^*=10.42. Further increased reduced velocity in the lower branch, at U^*=11.9, the total force phase (ϕ_{total}) also jumped and C_{total} and C_{vortex} are out of phase with the displacement signal. Hence, the following is observed:

Jump in ϕ_{vortex} between initial and upper branch

Jump in ϕ_{total} between upper and lower branch.

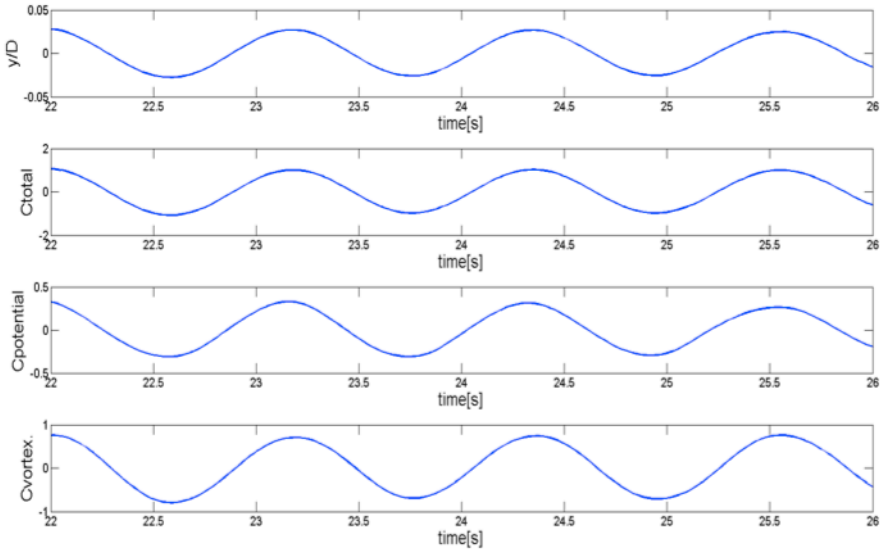

Fig. 3.12. Initial branch time histories at U^*=5.58

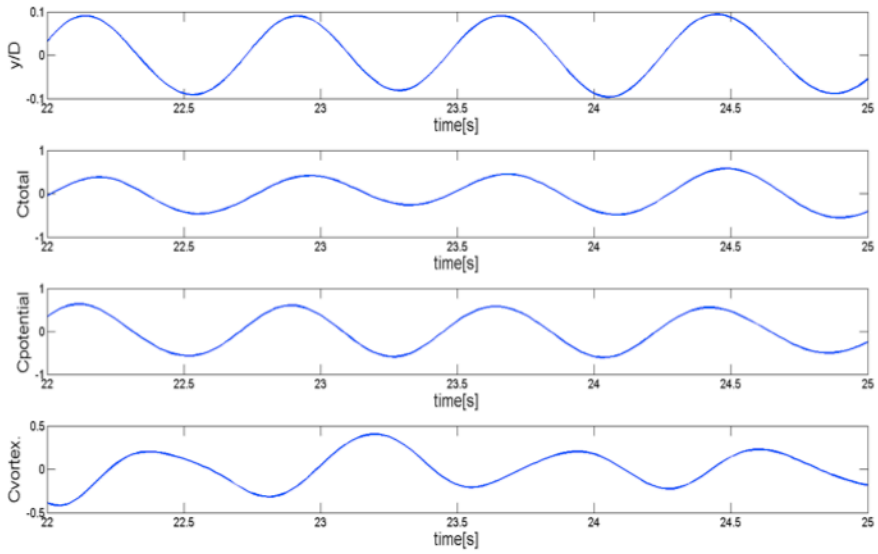

Fig. 3.13. Upper branch time histories at U^*=10.42

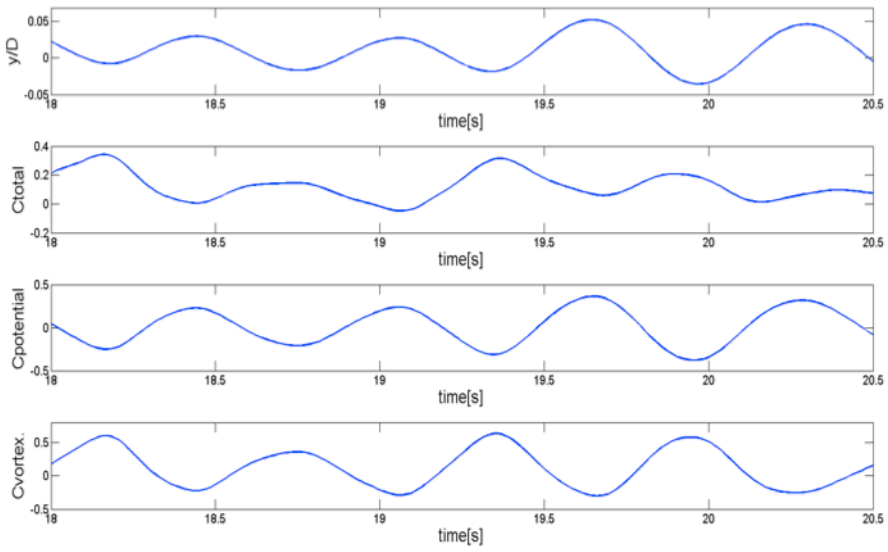

Fig. 3.14. Lower branch time histories at U^*=11.9

From calculated time histories of transverse force signals, the RMS (root mean square) method is used to average the C_{total}, and C_{vortex} at various reduced velocities. Phase angle between displacement and corresponding force signals are calculated by FFT (Fast Fourier Transform). In the frequency domain signal, a point where the body oscillation and the fluid force frequency are the same, is found and then the phase angle is calculated at this point. In addition, C_{total} and ϕ_{total} are calculated based on the analytical expressions suggested by Khalak and Williamson (1999). In their calculation, since they assumed that the cylinder displacement and fluid force are sinusoidal, their method is an approximation. By substituting equation (3.7) into the dimensionless equation of motion we have,

$$C_{total}\sin\phi = \frac{4\pi^3 A^*(m^* + C_A)\zeta}{(U^*/f^*)^2 f^*} \tag{3.17}$$

$$C_{total}\cos\phi = \frac{2\pi^3 A^*}{(U^*/f^*)^2} C_{EA} \tag{3.18}$$

$$f^* = \sqrt{\frac{m^* + C_A}{m^* + C_{EA}}} \tag{3.14}$$

Khalak & Williamson (1999) compared the C_{total} and ϕ_{total} found from direct measurement using a force sensor and approximate calculation based on the above equations for two values of m^*=3.3 and 10.1. The results clearly suggest that, at higher mass ratio (m^*=10.1) there could be significant difference between the calculated and the measured experimental values. But, at the same time, at lower mass ratio (m^*=3.3), the calculated and experimental values are very close. The m^* value of the present study is still lower (m^*=1.73) compared to Khalak & Williamson (1999). The discrepancy between the calculated values and the actual ones is expected to further narrow down or in other words, the calculated values of C_{total} and ϕ_{total} shown in Figs. 3.15 and 3.16 should closely represent the actual values.

Transvers force coefficient and phase angle found from the above method are presented in Figs. 3.15-3.18 along with Govardhan & Williamson (2000)'s result (m^*=8.63). As seen in Fig. 3.15, the inverse dynamics method and Williamson's approximation method matches very well. Since Williamson's method assumes sinusoidal motion, C_{total} in Williamson's method has slightly higher than that of the inverse dynamics method. From all three cases in Fig. 3.15, C_{total} shows an increasing trend with respect to U^* in the initial branch. As the reduced velocity increases, the maximum being at about U^*=6.0 at which the amplitude jumps from the initial branch to the upper branch. In upper branch, C_{total} of this study shows significant difference and have much higher and broader C_{total} than Williamson's results. This result coincides with the amplitude plot in Fig. 3.7. Present study has much higher amplitude and broader

upper branch region compared to Williamson. Hence, the maximum C_{total} is observed at the beginning of the upper branch and C_{total} is decreasing through the upper branch region. At the lower branch, C_{total} is almost constant and C_{total} is negligible at desynchronization.

The corresponding ϕ_{total} is seen in Fig. 3.16. The ϕ_{total} in the present study shows a very gradually increasing trend up to U^*=10.0 covering the initial and upper branches. Then ϕ_{total} abruptly jumps to much higher values in the lower branch at about U^*=11.0 as f_{osc} passes through f_N (1.4054 Hz) (Fig. 3.14). The jump in the lower branch is also seen in Govardhan & Williamson (2000) and the general trends of C_{total} and ϕ_{total} are similar. However, in general, for the initial and upper branches, the ϕ_{total} values in the present case are slightly higher than those of Govardhan & Williamson (2000), whereas, in the lower branch, ϕ_{total} values are slightly lower. Also, contrary to steady and nearly constant values reported by Govardhan & Williamson (2000), ϕ_{total} values of the lower branch exhibit significant fluctuations (by about 70°) corroborating with the greater modulations observed in the present study. The reason is that the lower branch in our study is brief and it looks more like desynchronization since at our high Re numbers the upper branch overtakes the lower branch and the cylinder displacement is irregular compared to Govardhan & Williamson (2000) where regular 2S mode was observed.

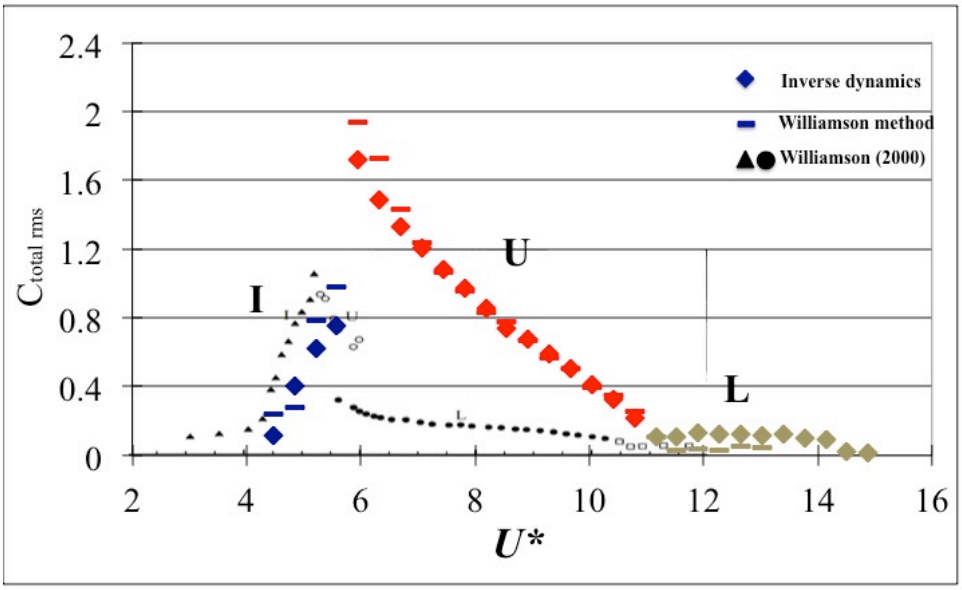

Fig. 3.15. $C_{total\ rms}$ vs. reduced velocity

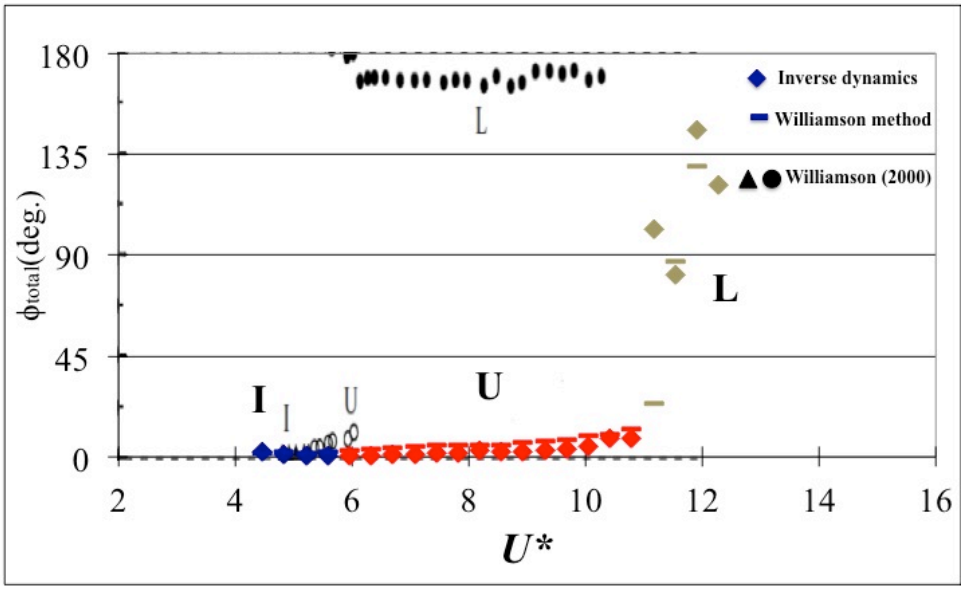

Fig. 3.16. ϕ_{total} vs. reduced velocity

Fig. 3.17 shows C_{vortex} at various reduced velocities. All three values match very well in initial branch with increasing trend. At the upper branch, C_{vortex} starts to decrease and then increase close to the lower branch. From the lower branch, C_{vortex} gradually decreases. In the present study, C_{vortex} has a maximum at the beginning of the upper

branch while Govardhan & Williamson (2000) results show a maximum C_{vortex} at lower branch. This is due to the fact that current study has much higher amplitude and broader upper branch regions than those of Govardhan & Williamson (2000). It is worthy to note that cylinder displacement is not only related to C_{vortex} but also ϕ_{vortex}. Govardhan & Williamson (2000) have maximum amplitude at the upper branch but maximum C_{vortex} is observed at the lower branch.

As seen in Fig. 3.18, ϕ_{vortex} is near 0° in the initial branch. ϕ_{vortex} in the upper branch response shows significant difference between the present study and Govardhan & Williamson (2000). At the upper branch, ϕ_{vortex} in the present study gradually increases up to $U^*\cong 8$. After f_{osc} passes through $f_{N,w}$ (1.118Hz) in the middle of the upper branch, ϕ_{vortex} jumps gradually to 180°, while ϕ_{vortex} of Govardhan & Williamson (2000) jump occurs at the beginning of the upper branch. The more gradual change in the present study is due to the higher system damping.

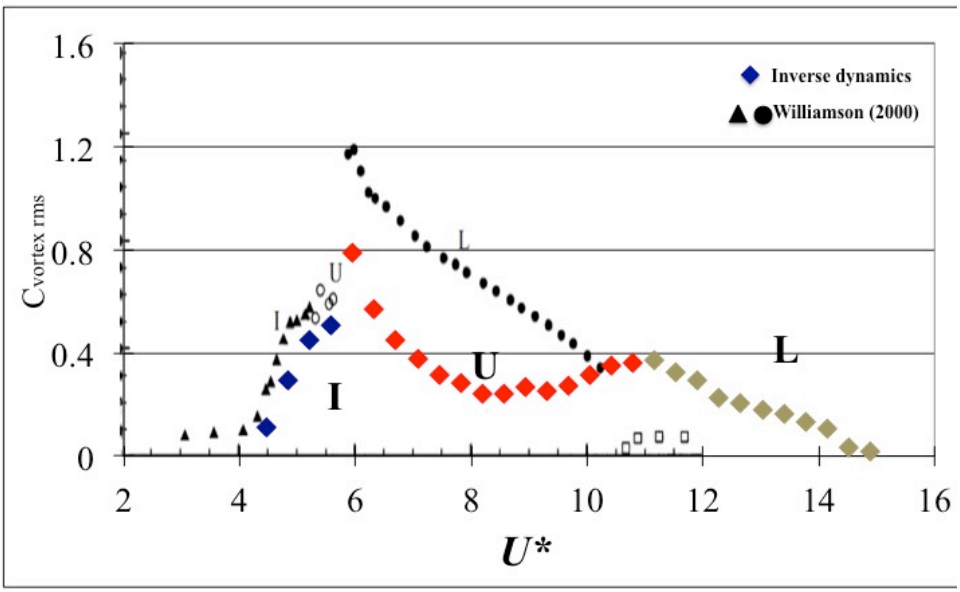

Fig. 3.17. $C_{vortex\ rms}$ vs. reduced velocity

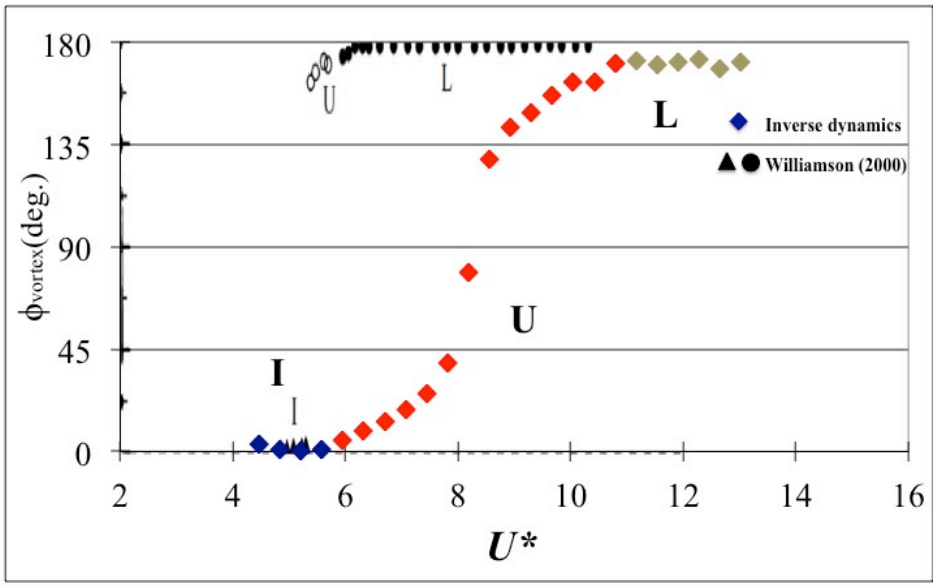

Fig. 3.18. ϕ_{vortex} vs. reduced velocity

3.2.4. Wake vortex structure

Near-wake vortex structures around the smooth cylinder are presented in this section. These are made out of the frame-by-frame analysis of the flow visualization videos made as a part of the present study. The flow structures are captured for cylinder motion over a complete cycle of oscillation starting from the Bottom Dead Center (BDC), which refers to the bottom most position of the cylinder in an oscillatory cycle, to the Top Dead Center (TDC) and back to BDC. The phase of cylinder motion is expressed in terms of t/T, where t is time and T is the period of oscillation. Only the salient features of the flow structures are illustrated. It should be noted that the sketches of flow patterns presented are drawn not to scale as they are primarily meant to bring out the qualitative aspects of the flow fields and not any quantitative measures. In all cases, the wake structures are captured within a downstream distance of about 4.0*D*. A few actual pictures of flow

visualization with broad field-of-view (FOV) to capture the near wake are added when an important wake feature cannot be described clearly in a sketch.

Typical flow structures are presented here for the initial, upper, and lower branch and also the desynchronization. The range of Reynolds number for the tests is $3\times10^4 \leq Re \leq 1.2\times10^5$.

3.2.4.1. Initial branch

Initial branch commences with the 2S mode of shedding and it starts at U^*=4.84. It is not presented here since it is a well-known mode of vortex shedding. As the reduced velocity is increased, at U^*=5.58, i.e. at the upper end of the initial branch, it is found that 3 vortices are shed per cycle of oscillation, and the non-dimensional amplitude A^* is 0.404. The vortex pattern observed in a typical oscillatory cycle is given in the sketch sequence in Fig. 3.19. The vortices are numbered (e.g., V1, V2), in the order of their initial genesis while still attached to the cylinder. This order may be different from the order of shedding. Thick and dashed flow lines marked in the flow fields indicate flow of fluid carrying oppositely signed vorticity across the wake.

As Fig. 3.19 shows, starting from BDC (Fig. 3.19(a)), the bottom shear layer produces two vortices V1 and V2 (V2 is borne at BDC, whereas V1 was borne earlier) coalescing to form a larger vortex V1,2 at t/T=0.167 (Fig. 3.19(c)). In the meanwhile, another vortex V3 was borne at t/T=0.084 (Fig. 3.19(b)) growing as the cylinder moves up towards TDC. V3 undergoes limited growth due to the presence of the stronger vortices V1,2 and Vx (formed in the previous cycle) in Fig. 3.19(b). V3 is shed at

t/T=0.375 (Fig. 3.19(f)) due to the 'passive pushing' by its co-generated (same shear layer) vortex V5. This passive shedding mechanism was first observed for a square section cylinder (Kumar et al. 2009). After significant growth, V1,2 is shed at t/T=0.417 (Fig. 3.19(g)). Shedding of V1,2 occurs partly due to the action of fluid carrying oppositely signed vorticity (following the mechanism described by Gerrard 1966) and partly due to the passive pushing provided by V4. At TDC, the top shear layer gives genesis to a new vortex V6 (Fig. 3.19(i)) which coalesces with V5 to form V5,6 at t/T=0.667 (Fig. 3.19(l)). V4 borne at t/T=0.292 steadily grows and rolls over the cylinder towards its base reaching much bigger than usual size and shedding in next cycle after V5,6. Vortex V5,6 sheds at t/T=0.875 (Fig. 3.19(o)). Hence, 3 vortices (V1,2, V3, and V5,6) shed per oscillatory cycle with no pairing between the shed vortices; for Re≅43,300 and A^*≅0.4. This shedding pattern is different from the 2S mode observed by Williamson & Roshko (1988) for Re≅1,000 and A^*≅0.4. and extended to Re≅3,500-10,000 (Khalak & Williamson, 1999).

The wake inclination angle in Figs. 3.19(j)-(l) clearly does not follow the direction of the relative flow velocity. Starting from TDC (Fig. 3.19(i)), it takes about 0.25T for the wake to align itself to the direction of the relative flow velocity. In other words, there is a phase lag of about 90° for the wake swing, which suggests the existence of wake inertia.

In the present case, f_{osc}/f_s =0.64, where f_{osc} is the oscillation frequency and f_s is the Strouhal frequency for a stationary cylinder. It should be noted that at the same Reynolds number Re≅4.33×10^4 for a small difference in reduced velocity (U^*≅5.60) but at a higher value of f_{osc}/f_s=0.74, the vortex structure observed by Chang et al. (2011) included shedding of 7 individual vortices per cycle (Fig. 3.20). Distinct differences are observed

between Figs. 3.19 and 3.20. At BDC itself, a different flow structure is shown in Fig. 3.20(a) where the bottom shear layer forms only V2 whereas in Fig. 3.19(a) two vortices V1 and V2 grow which eventually coalesce to form a V1,2 as mentioned earlier. Similarly, the top shear layer in Fig. 3.20(a) grows vortex V1 whereas in Fig. 3.10(a) the fully grown vortex Vx is shed from the top shear layer. At t/T=0.1817 (Fig. 3.20(b)), an additional vortex V3 rolls up on top of V1 (total of two vortices in top shear layer) which is not observed in Figs. 3.19(c)-(d). In Figs. 3.19(c)-(d), the flow structures at t/T=0.167 and t/T=0.274 are quite similar and hence, the flow structure, at an intermediate time instant t/T=0.1817 (which is not shown in Fig. 3.19), should be nearly identical with two vortices constituting the near-wake. Clearly, the third vortex V3 (2^{nd} vortex in top shear layer) in Fig. 3.20(b) does not exist in Fig. 3.19(c)-(d).

In a similar manner, flow structure at t/T=0.773 (Fig. 3.20(g)) should be identical to the wake vortex structures shown at t/T=0.751 in Fig. 3.19(m), and at t/T=0.792 in Fig. 3.19(n). However, the wake vortex structures in Fig. 3.20(g) are distinctly different from Figs. 3.19(m)-(n). This shows that, the near-wake vortex structures are sensitive to the ratio, f_{osc}/f_s as also observed by previous investigators at lower Reynolds numbers (Ongoren & Rockwell, 1988). From the results, it could be inferred that, the vortex structures around the cylinder is a function of reduced velocity (U^*), oscillation frequency ratio (f_{osc}/f_s) and also the Reynolds number.

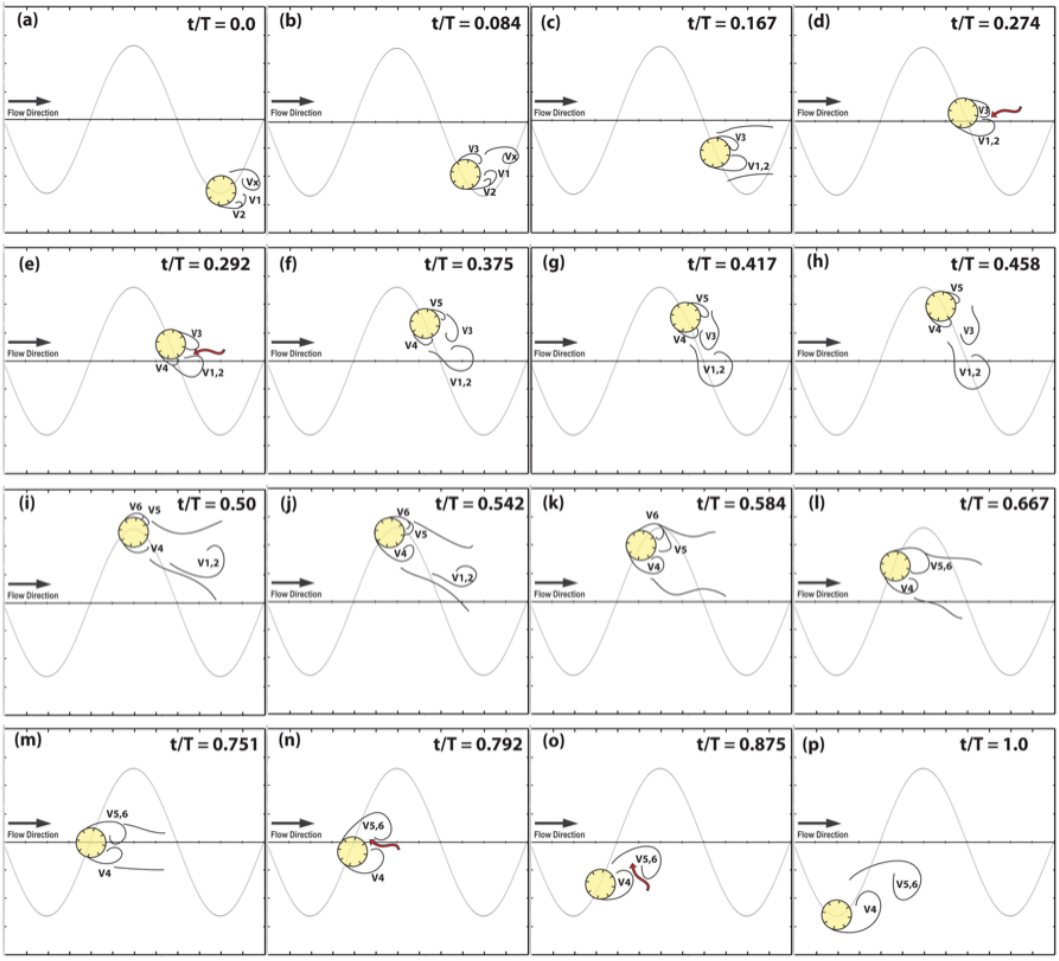

Fig. 3.19. Wake vortex structure of smooth cylinder over a cycle:U^*=5.58 (upper end of initial branch), Re=4.33×10^4, A^*=0.404, f_{osc} /f_s =0.64.

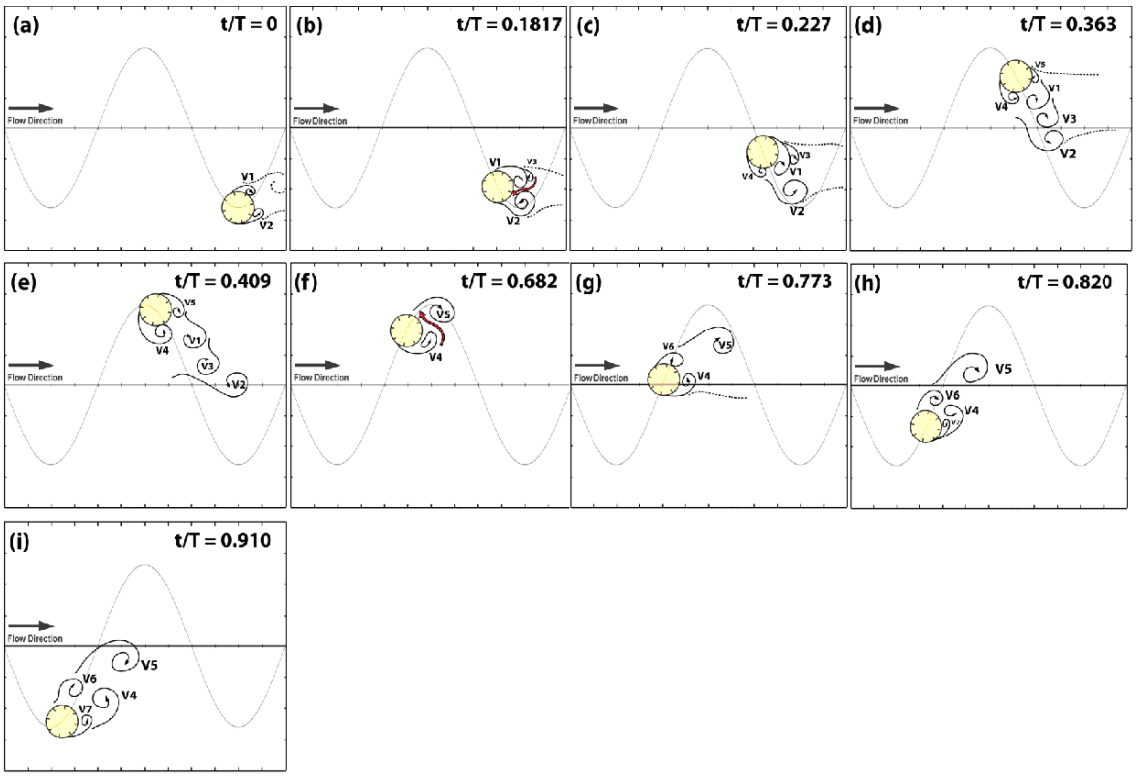

Fig. 3.20. Wake vortex structure of smooth cylinder over a cycle: U^*=5.6 (upper end of initial branch), Re=4.33×10^4, A^*=0.443, f_{osc} /f_s =0.74 (Chang et al. 2011)

3.2.4.2. Upper branch

As the reduced velocity is increased, the upper branch is reached and different vortex patterns are observed. Fig. 3.21 shows flow structure 2P+S around the cylinder at U^*=8.18 for Re=63,500 and A^*=1.39.

Starting from BDC, during the upward travel of the cylinder, vortices V1 (shed at t/T=0.278; Fig. 3.21(d)) and V2 (shed at t/T=0.111; Fig. 3.21(b)) form a pair as is evident at t/T=0.278. A second pair of vortices is formed by V3 (shed at t/T=0.723; Fig. 3.21(h)) and V4 (shed at t/T=0.50; Fig. 3.21(f)) at t/T=0.723. Additionally, a single vortex V6 is shed at t/T=1.0 (BDC). In this case, the vortices V4 and V6 are shed by the action of oppositely signed vorticity, i.e. following Gerrrad's mechanism, whereas V1 and V2 are

shed due to the operation of both 'passive pushing' mechanism and Gerrard's mechanism. For V3, passive pushing by V6 appears to be the sole mechanism inducing shedding. Thus, the mode of vortex shedding observed is 2P+S (V1, V2, V3, V4, and V6).

It should be noted that, the 2P+S mode is observed in the 'no-synchronized pattern zone' of the Williamson-Roshko map for 300<Re<1000 (Fig. 3(a) of Williamson & Roshko 1988). The differences in wake vortex structures reported in this paper are the effect of higher Reynolds numbers.

At a lower reduced velocity of U^*=6.32 (upper branch), the same mode of shedding is observed for the majority of the oscillatory cycles analyzed but without vortex pairing in few cycles of oscillation. That is, in few oscillatory cycles, vortices are not pairing up possibly due to the difference in their convection velocities. A close examination of flow structures reveals that vortices with near-equal convection velocities possibly pair-up provided their shedding timings are appropriate. Apart from these factors, vortex-vortex interactions appear to have been influenced by wake deflections.

In the upper end of the upper branch, at a still higher reduced velocity (U^*=10.42), the 2P+2S mode of shedding is observed in few oscillatory cycles. That is, one additional vortex is shed (either by the top or the bottom shear layer) in some cycles of oscillation giving rise to the 2P+2S mode of shedding. This additional vortex is shown in Fig. 3.22 where vortex V3 is the additional vortex formed in the top shear layer contributing to 2P+2S mode (see Fig. 3.21(g) for comparison). On closer inspection, it is also noticed that, in those cycles with 2P+2S shedding mode, the vortices are in generally larger (stronger) when compared to those at lower reduced velocities. Thus, it is conjectured

that, the amount of vorticity generated and shed at this reduced velocity (U^*=10.42) is higher, which is rightly reflected in the higher amplitude of oscillation observed in this case (Fig. 3.7).

The vortex pairs after formation are observed to traverse in the direction of the wake axis (which is skewed many a times due to wake deflections). It is pointed out that, in a vortex pair, the size of participating vortices are not always the same. Many a times, they are identical but sometimes, notable size difference was observed between them. In the upper branch, at higher reduced velocities, higher wake deflections (wake swings) are observed. Such wake swings (but with lower angle of swing) have been reported by Ongoren & Rockwell (1988) also even at lower Reynolds numbers.

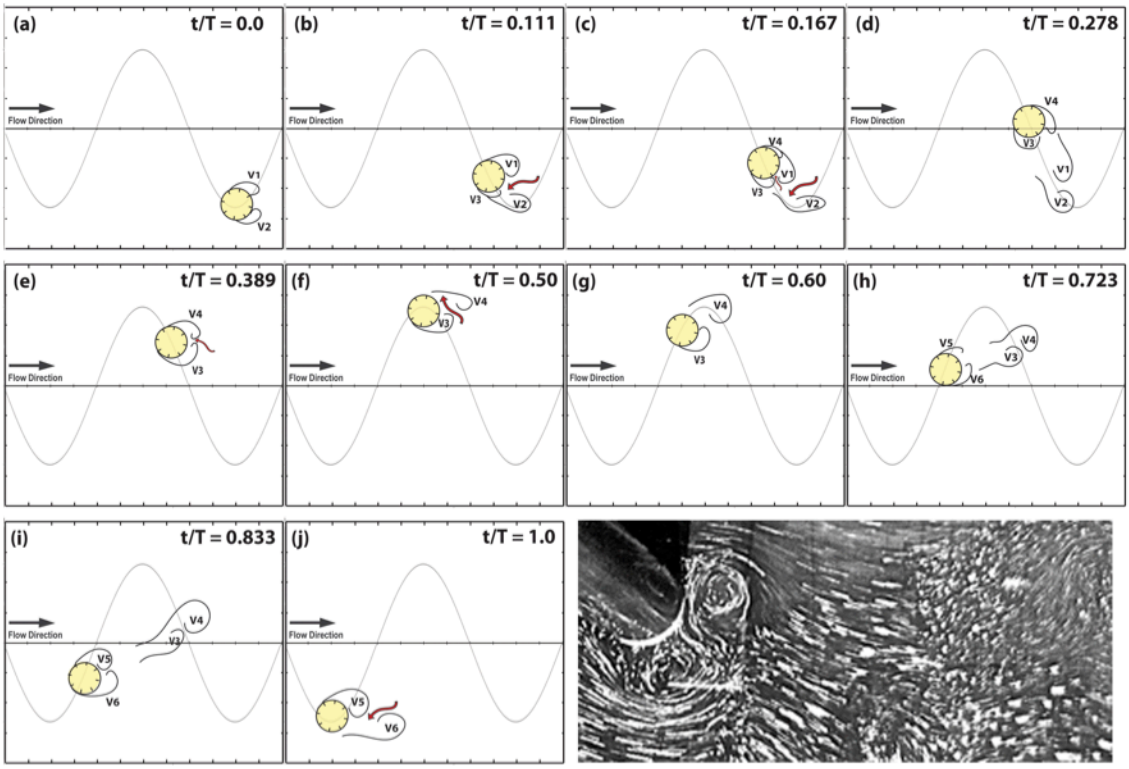

Fig. 3.21. Wake vortex structure of smooth cylinder over a cycle: U^*=8.18 (upper branch), Re=6.35×10^4, A^*=1.39; 2P+S pattern; visualization picture shows the moment between (e) and (f)

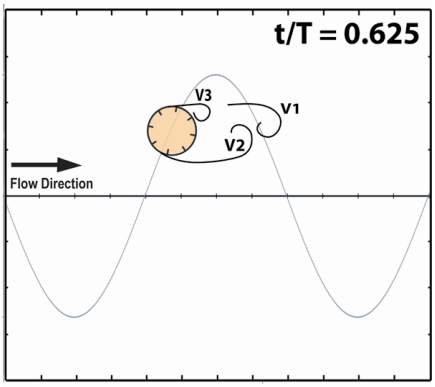

Fig. 3.22. Wake vortex structure of smooth cylinder for U^*=10.42 (upper branch), Re=8.08×10^4, at t/T=0.625: A^*=1.57, larger vortices compared to Fig. 3.21(h), pattern 2P+2S(U^*=10.42) vs. 2P+S (U^*=8.18)in Fig. 3.22

3.2.4.3. Lower branch

In the lower branch, notable cycle-to-cycle variations have been observed in the wake vortex structures. For the majority of cycles, about 7 individual vortices are shed per cycle of oscillation. However in most cases, the vortices were very weakly rolled up and quickly dissipated in the wake. Flow structures around the cylinder for a typical oscillatory cycle with U^*=12.28 are presented in Fig. 3.23. At BDC, vortex V1 borne in the previous cycle grows and sheds at Fig 3.23(c). As the cylinder progresses its upward motion from BDC, vortex V2 borne in the bottom shear layer shortly after BDC (at t/T=0.039; Fig. 3.23(b)) and is shed at t/T=0.31 (Fig. 3.23(f)). In the meanwhile, another weak (less circulation) vortex V3 (formed at t/T=0.153) quickly dissolves into the wake at t/T=0.231. Two new vortices V4 and V5 were borne simultaneously at t/T=0.31 (Fig. 3.23(f)), after exhibiting some growth, shed at t/T=0.655 and t/T=0.462, respectively.

Two more vortices are shed in this cycle, namely V6 (shed at t/T=0.577) and V7 (shed at t/T=0.886). Among all the vortices, only V7 is comparatively stronger but still weaker (less circulation) when compared to the vortices shed in the upper branch. Thus, a total of 7 vortices (V1, V2, V3, V4, V5, V6, and V7) are shed per cycle of oscillation.

There is cycle-to-cycle variation in the wake structures as can be surmised by comparing Fig. 3.24(a) (cycle 2) to 3.23(f) (cycle 1) and Fig. 3.24(b) (cycle 3) to 3.23(i) (cycle 1). These are three different cycles occurring during the same test at constant U^*. This observation indicates that the body oscillation is not synchronized with the vortex shedding process, which is clearly reflected in the corresponding displacement time histories of the body motion. Examples of such times histories and corresponding spectra were shown in Figs. 3.8(e) and 3.8(f).

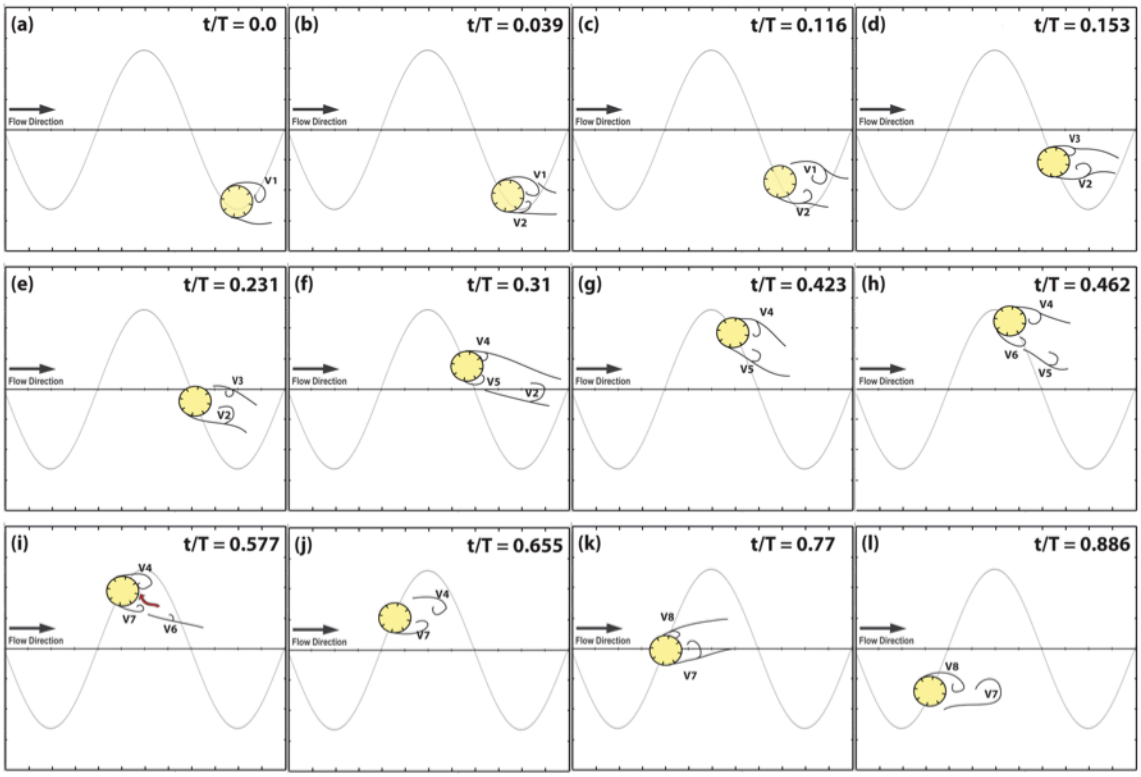

Fig. 3.23. Wake vortex structure of smooth cylinder over a cycle: U^*=12.28 (lower branch), Re=9.53×10^4, A^*=0.76

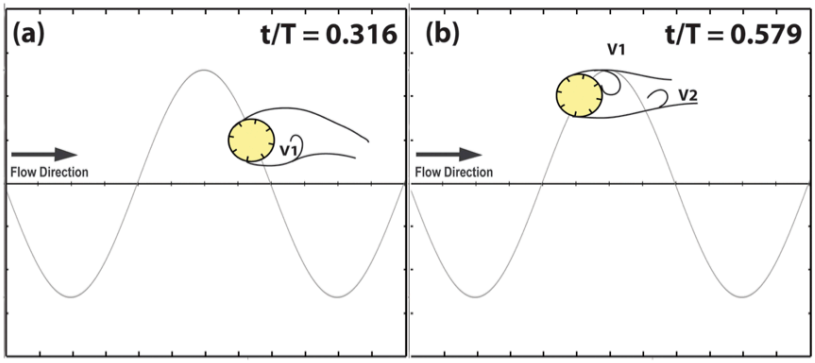

Fig. 3.24. Variation of instantaneous wake vortex structure of smooth cylinder: U^*=12.28 (lower branch), Re=9.53×10^4, A^*=0.76; (a) Cycle C2, (b) Cycle C3

3.2.4.4. Desynchronization

In the desynchronization, no definite periodicity is observed in the wake of the cylinder indicating that the shedding process is completely unlocked from the cylinder motion. Frequently in desynchronization, vortex shedding is completely suppressed in the range of Reynolds number studied in this paper. Instead of a von Kármán Street, a wake with two attached vortices symmetric about the wake axis is developed as shown in Fig. 3.25(a) (U^* = 14.5). Also, the wake is short and narrow while the vorticity generated is defused via a narrow trail of small-scale vorticity as shown in Fig. 3.25(b). This results in near-equal pressure distribution on the top and bottom surfaces of the cylinder, inducing negligible lift force and consequently small amplitude motion. Generally in this case, the vortices are weakly rolled up rightly reflecting the smaller excitation amplitudes observed (Fig. 3.7).

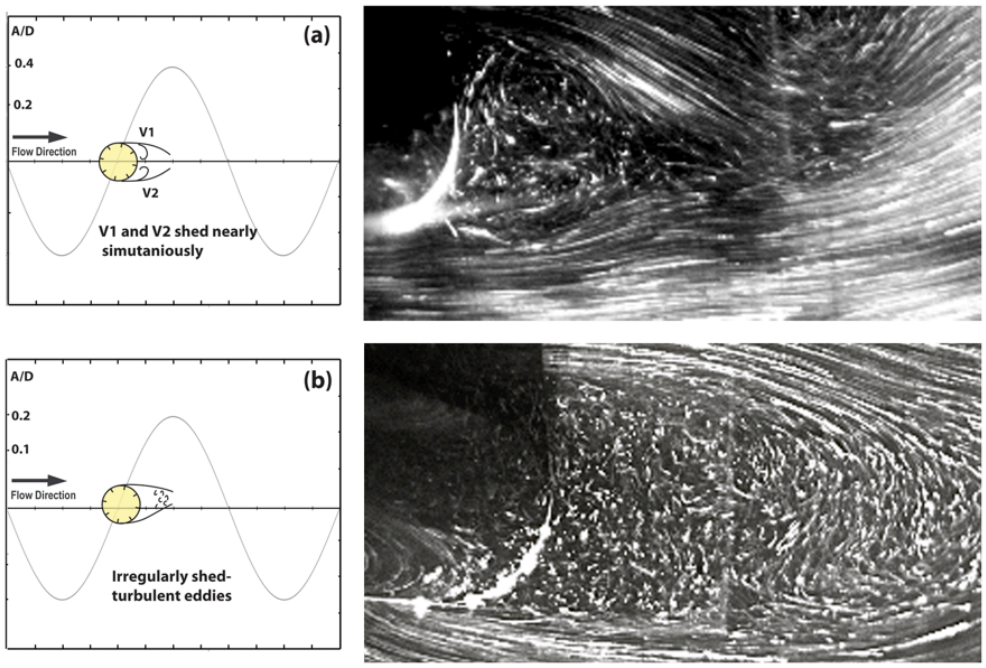

Fig. 3.25. Typical wake vortex structure of smooth cylinder at U^*=14.51 (desynchronization), Re=1.12×10^5, A^*=0.06

3.3. MAIN FINDINGS

Based on the results presented in this section, the following conclusions for the FIM of a smooth cylinder are drawn for Reynolds number in the range 3×10^4<Re<1.2×10^5 which primarily covers the high-lift TrSL3:

(i) The upper branch in the present study is the broadest part of the VIV synchronization and the branch where the highest amplitude is observed.

(ii) The lower branch is very narrow and has been overtaken by the upper branch in comparison to low Re VIV.

(iii) The response in the sloping lower branch is classified as a 'mixed response' falling between the conventional (low Re) lower branch with steady, periodic

oscillations and desynchronization characterized by random on-off VIV time-intervals. That is, it has both the characteristics of a conventional steady lower branch and desynchronization. This is also the effect of much higher Reynolds numbers used in the present investigation.

(iv) From phase difference between the cylinder motion and vortex force, ϕ_{vortex} jump is observed between initial and upper branch same as Govardhan & Williamson (2000). However, due to mixed property of lower branch in the present study, C_{vortex} has maximum value in the upper branch different from Govardhan & Williamson (2000) result where lower branch has maximum C_{vortex}.

(v) From phase difference between the cylinder motion and total force, ϕ_{total} jump is observed between upper and lower branch. Since lower branch response in the present study is not steady and stable, ϕ_{total} has modulation after jump. From Govardhan & Williamson (2000), C_{total} has maximum value in the lower branch. Because of much broad response region and much high amplitude motion in the upper branch than that of Govardhan & Williamson (2000), C_{total} has maximum value in the upper branch and maximum C_{total} is 36% higher than the result by Govardhan & Williamson (2000).

(vi) For a smooth cylinder, the 2S structure is observed at the beginning of the initial branch. Due to the higher Reynolds number range considered in this study, non-conventional wake vortex structures are found following the end of the initial branch. At the end of the initial branch, 3 individual vortices are shed. In the upper branch, the 2P+S structure is observed. At the end of upper branch where maximum amplitude occurs, occasionally the 2P+2S structure with generally